First-principles Modeling of Anode/Electrolyte Interfaces in Beyond Li-ion Batteries

by

Jeffrey S. Lowe

A dissertation submitted in partial fulfillment
of the requirements for the degree of
Doctor of Philosophy
(Chemical Engineering)
in the University of Michigan
2019

Doctoral Committee:

Assistant Professor Heather Mayes, Co-Chair
Associate Professor Donald Siegel, Co-Chair
Assistant Professor Neil Dasgupta
Professor Johannes W. Schwank

Jeffrey S. Lowe

jefflowe@umich.edu

ORCID iD: 0000-0002-0816-9105

Acknowledgements

I first want to acknowledge the financial support. This work was supported by the Joint Center for Energy Storage Research, an Energy Innovation Hub funded by the U.S. Department of Energy, Office of Science, Basic Energy Sciences, and by the U.S. National Science Foundation. In addition, the University of Michigan provided funding for me to present this work at external conferences.

I want to thank my committee members Professors Heather Mayes, Neil Dasgupta, Johannes Schwank, and my advisor Prof. Don Siegel for providing feedback and guidance on my dissertation. I especially want to thank Prof. Don Siegel for all the years of guidance during my dissertation work. He set a great example for a faculty member to excel both in research and in teaching. All of my current and former research group members, particularly those that I have collaborated with on publications: Dr. Jason Lai, Dr. Alauddin Ahmed, Steven Kiyabu, and Dr. Nitin Kumar. I want to acknowledge Alauddin Ahmed for all of his support; he has shown me the path towards an academic position. Special thanks to all of the other chemical engineering graduate students who lifted me up along the way and with whom I have formed lifelong friendships.

The wonderful faculty and staff who have supported me both formally and informally. They're the people that make the University of Michigan the great place that it is. The Chemical Engineering Graduate Coordinator Susan Hamlin, the Coordinator of Graduate Programs in the College of Engineering Andria Rose, the Director of Undergraduate Studies, Undergraduate Program Advisor, and wonderful mentor Dr. Susan Montgomery, and so many others. In particular, I want to thank Dr. Montgomery for mentoring me in teaching and in all the informal areas that often go undiscussed in the academy, but that have been so crucial in my development as a researcher.

Finally, and most importantly, I would like to give a heartfelt thanks to my family. My wife Alex Rafalski has been very supportive of me throughout this process. I want to thank her for every sacrifice that she's made along the way, and for everything she's done to help me get to the finish line. From taking on more chores when my work schedule was busy to giving me encouragement at difficult times. I also want to thank my entire family, especially my parents Chris and Diane

Lowe, my sister Amy Cirillo, and my brother Nicholas Lowe. They have supported me unconditionally my whole life and have always encouraged me to follow my passions. This dissertation was only possible because of them.

Table of Contents

List of Tables

List of Figures

Abstract

A societal shift towards greater adoption of renewable energy is underway. To accelerate this transition, new approaches for energy storage are needed to address the intermittent nature of these resources. Batteries are amongst the most promising energy storage devices. State-of-the-art lithium-ion (Li-ion) batteries are beginning to be deployed in applications such as transportation and for grid energy storage. However, Li-ion technologies have yet to be applied widely in these applications due to their limited energy storage capacities. Promising next-generation battery chemistries, such as magnesium (Mg) and lithium metal batteries, have the potential to improve capacities by as much as an order of magnitude over current Li-ion cells. However, metallic anode materials suffer from detrimental interactions with the battery electrolyte.

This dissertation analyzes the unique challenges for Mg and Li metal batteries at the anode/electrolyte interface using first-principles computation. In Mg metal batteries, a key challenge is electrolyte decomposition at the Mg anode surface. DFT calculations are performed to predict both the thermodynamic driving force and kinetics of plausible decomposition reactions of DME, a common solvent, on three Mg anode surface phases: Mg metal, MgO, and $MgCl_2$. DME is predicted to rapidly decompose to ethylene gas and other products on the metallic Mg surface, whereas the presence of an oxide or chloride surface film on a Mg anode is predicted to limit solvent decomposition. The stability of the Cl-based surface may explain how Cl additions to an electrolyte contribute to improvements in the anode performance via a Mg−Cl enhancement layer.

In Li-based batteries, a solid electrolyte interphase (SEI) layer is known to form on the anode, but the detailed composition and structure of the SEI, along with its evolution upon battery cycling, remains a matter of debate. In batteries that use metallic lithium as an anode, dendrite formation during Li plating presents an additional and major failure mode. These challenges are addressed from two angles. First, one potential solution to these challenges is to employ a protective membrane at the Li anode. For such membrane to function, strong adhesion or wetting of the membrane by Li must occur. Using first-principles calculations, the adhesive properties of graphene oxide (GO), a promising membrane material, are investigated at an interface with

lithium. These calculations indicate that Li strongly adheres to the GO surface, supporting the use of GO as a protective layer.

Second, although the composition of the SEI varies across electrolytes, the native oxide Li_2O is an omnipresent component that comprises the innermost SEI layer in virtually any battery employing a Li metal anode. Despite its ubiquity, the properties of this native oxide layer, and its interface with underlying Li metal, have not been widely examined. Here rigorous, first-principles models of the native oxide layer on Li metal are developed. Two models are constructed and analyzed: an ideal crystalline interface, and an amorphous model in which the oxide layer is 'grown' by step-wise oxidation of Li metal. Quantitative analyses are presented that distinguish the change in electronic structure of Li atoms across the interface, differentiating metallic Li and oxidized Li ions. Finally, Li-ion diffusivities within the oxide are computed; the data support the fast transport of Li ions through the oxide layer. In total, these calculations provide a highly detailed description of the structural, transport, and mechanical properties of the Li/Li_2O interface.

Chapter 1: Introduction

1.1 Beyond state-of-the-art Li-ion batteries

As we move further into the 21st Century, one of the largest challenges faced by our nation is in energy storage. Energy consumption is increasing, fossil fuels are being depleted, and an increased importance is being placed on obtaining and storing energy through environmentally friendly means. Due to these factors, a societal shift towards greater adoption of renewable energy is underway. To accelerate this transition, new approaches for energy storage are needed to address the intermittent nature of these resources. Among the most promising devices for energy storage are batteries. In the last two decades, lithium-ion (Li-ion) batteries have revolutionized the consumer electronics industry. Li-ion batteries are well-suited for consumer electronics due to their ability to provide moderate energy densities in a relatively small package. Li-ion batteries have also begun to be applied to applications requiring higher energy densities, such as in transportation vehicles and for grid energy storage. However, Li-ion technologies have yet to be applied widely in these applications.

One of the main roadblocks for the adoption of Li-ion technologies in these new applications is the capacity. Current Li-ion batteries employ graphite as the negative electrode, or anode, material. Lithium ions are stored in the graphite anode by intercalation in between sheets of graphene. When the battery is charged and discharged, Li ions move into and out of the graphene sheets, respectively. Because the graphite is not able to be cycled during charge and discharge, it can be thought of as "dead weight." One approach for achieving batteries with higher capacities is to replace the graphite anode with a metal, such as lithium or magnesium (Mg). In this setup, all of the metal in the anode, in principle, can contribute to usable capacity in the battery since all of the metal can be plated and stripped during charging and discharging (Figure 1.1).

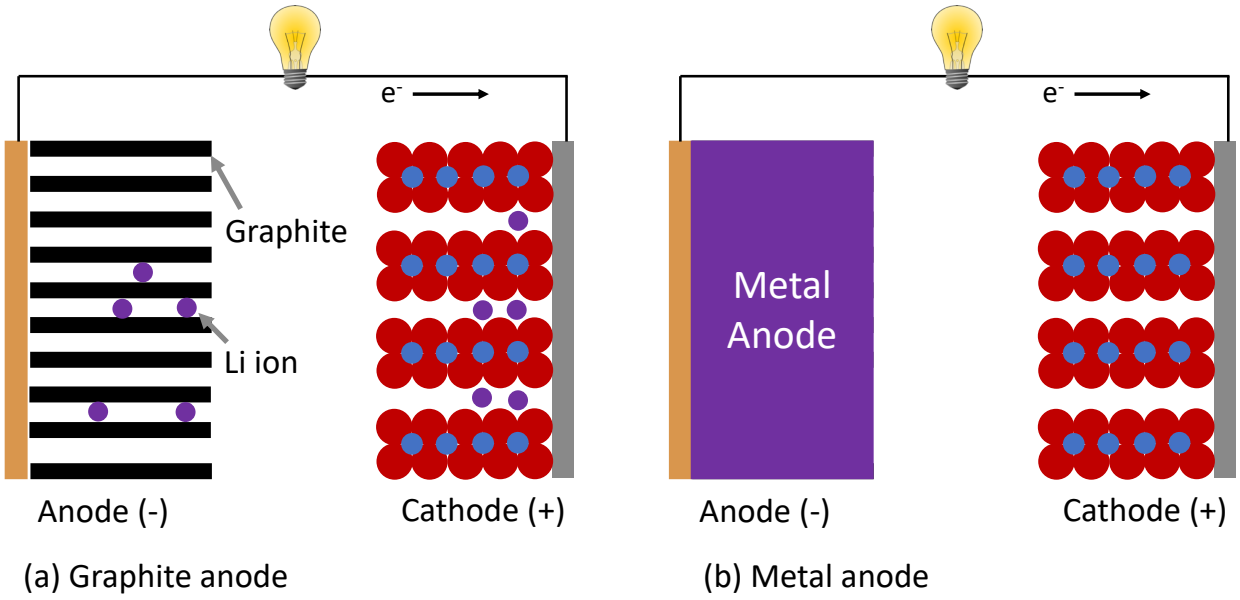

Figure 1.1 Li-ion cell schematics. (a) Current state-of-the-art Li-ion battery with a graphite intercalation anode, and (b) a battery with a metal anode. The latter represents a battery with a higher theoretical capacity since all of the metal in the anode contributes to the usable battery capacity.

Replacing the graphite intercalation anode with a metallic anode has the potential to substantially improve theoretical energy capacities. The capacities of two of the most promising metallic anodes, lithium and magnesium, are compared with graphite in Table 1.1. Theoretical capacities are improved by as much as an order of magnitude when moving to metal anodes. Li metal anodes show the largest gravimetric capacity due to the small mass of a Li ion. Yet, Mg metal anodes display the largest volumetric capacity given that the ionic radius of a Mg ion is similar to that of a Li ion, but the divalent Mg^{2+} transfers twice the amount of charge as compared to the monovalent Li^{+}.

Table 1.1 Theoretical capacities for promising metallic anode materials in comparison to a graphite anode in state-of-the-art Li-ion batteries.[1]

Anode	Volumetric capacity (mAh/cm^3)	Gravimetric capacity (mAh/g)
Graphite (LiC_6)	837	372
Li metal	2061	3862
Mg metal	3832	2205

Taking into account the discharge reaction at the cathode, the theoretical energy density of a battery system can also be computed. A summary of computed theoretical gravimetric energy densities for a variety of battery systems, including a number of systems employing Li and Mg metal anodes, is displayed in Figure 1.2. In general, Li metal systems appear to be the most

promising, with Mg metal systems also showing relatively high energy densities. As with capacity, the energy densities of Mg metal systems are even more promising on a volumetric basis. Therefore, although the numerical values discussed are on a theoretical basis and real battery systems will display lower energy densities, batteries with Mg and Li metal anodes are valuable systems for further study.

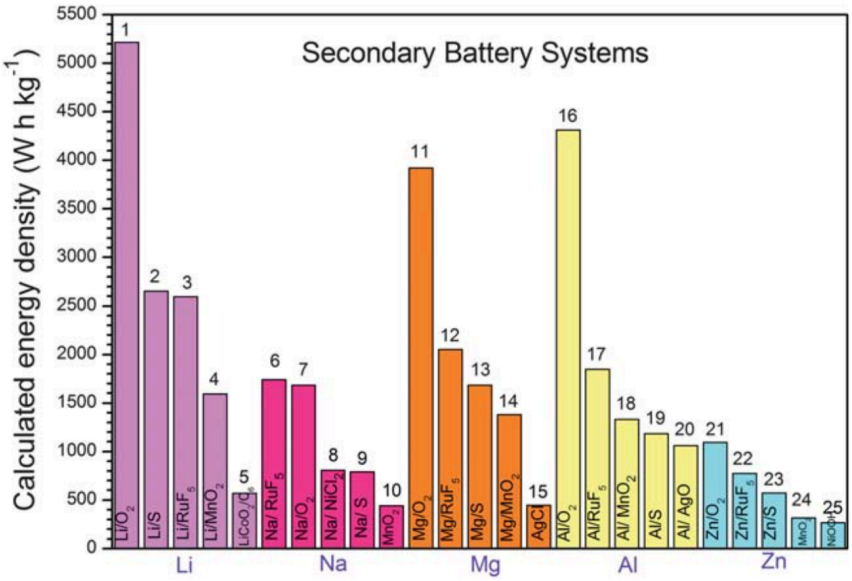

Figure 1.2 Theoretical gravimetric energy densities of various battery systems employing metal anode materials. Taken from Zu and Li.[2]

1.2 Metallic anode/electrolyte interfaces

Nonetheless, metallic anodes introduce new challenges for battery operation, which are governed by the interface that forms between the anode and the electrolyte. Specifically, an electrochemical or a chemical reaction may occur between the anode and the electrolyte. An electrochemical reaction involves a transfer of electrons between the anode and the electrolyte. If the Fermi level of a metallic anode is higher in energy than the lowest unoccupied molecular orbital (LUMO) energy level in the electrolyte, then electrons will be transferred from the anode to the electrolyte, reducing the electrolyte. See Figure 1.3 for a diagram showing electrochemical stability conditions.

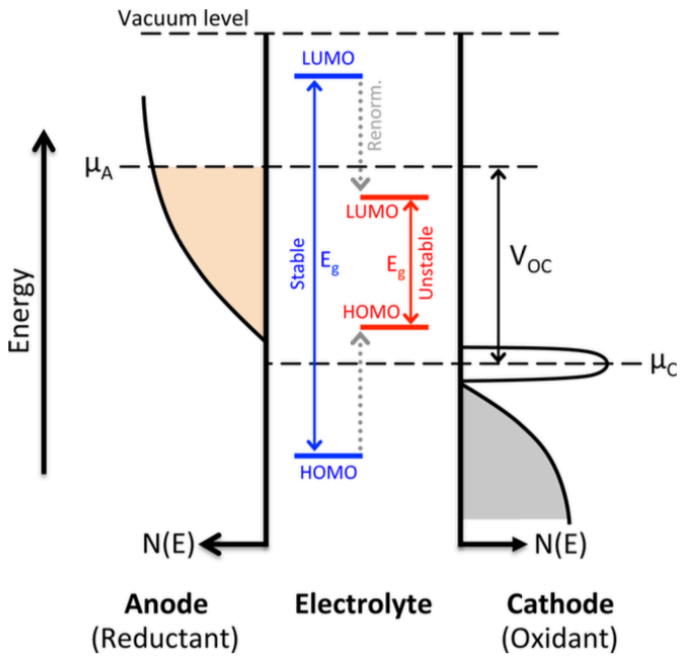

Figure 1.3 Conditions for anode/electrolyte electrochemical stability. If the LUMO level of the electrolyte is above the Fermi level of the metallic anode, the electrolyte is stable with respect to electrochemical reduction by the anode. This condition is illustrated in blue. An unstable electrolyte is illustrated in red. Taken from Kumar and Siegel.[3]

In a chemical reaction, species present in the electrolyte decompose to species of new chemical compositions on the anode surface. This process is governed by a thermodynamic driving force (i.e., the decomposed products are lower in energy than the original species in the electrolyte). Both electrochemical and chemical reactions result in decomposition of the electrolyte and the formation of a new surface layer on the anode. This surface layer is commonly referred to as the solid electrolyte interphase (SEI) layer. In current Li-ion cells, a standard electrolyte is a carbonate solvent with a $LiPF_6$ salt. In these cells, the LUMO level is lower in energy than the Fermi level of the graphite anode, resulting in reductive decomposition of the electrolyte on the anode surface and the formation of an SEI.[4,5] However, this electrochemical decomposition is self-limiting in current Li-ion cells. After the formation of an SEI during initial charge/discharge cycles, a stable SEI layer is formed that prevents further electrolyte decomposition.

In batteries with metallic anode materials, the nature of the SEI, due to its complexity, remains unknown.[6] The SEI is of critical importance as it prevents further electrolyte decomposition, but also must allow metal cations to be transported across its thickness during battery operation. Thus, one of the main challenges associated with the implementation of metallic anodes in next-generation batteries is an improved understanding of the nature of the SEI layer in these battery

chemistries. As the anode/electrolyte interface is highly dependent on the system being considered, this interface will be addressed in the context of specific systems in the following sections.

1.3 Magnesium metal batteries

In past work, the electrochemical stability of a Mg anode with respect to a set of common electrolytes was assessed.[3] Although the LUMO levels were generally found to decrease due to the adsorption of a solvent molecule on a surface, the LUMO energy was above the Fermi level of the anode in all cases studied. This finding implies that the Mg anode is stable to electrochemical reaction. The susceptibility of a Mg anode to chemical reaction, on the other hand, has yet to be addressed. Whether or not a Mg anode is likely to chemically react with the electrolyte is a key question. It has been suggested that the degradation of salt or solvent species present in the electrolyte forms a layer blocking the transport of Mg^{2+} across the electrode – electrolyte interface.[1,7,8]

To prevent the formation of a Mg^{2+}-blocking layer, many studies focus on electrolytes that can reversibly plate and strip Mg at the negative electrode.[8–13] Among the most promising solvents are ethereal solvents such as tetrahydrofuran (THF) and various glymes. Nonetheless, even when employing solvents that have been demonstrated to support reversible plating and stripping of Mg, there is evidence of electrolyte decomposition occurring. A number of experimental studies have observed variability in electrochemical performance after holding ethereal solvent-based cells at open circuit voltage (OCV).[9,14–16] For instance, Tutusaus *et al.*[15] observed increased polarization and higher interfacial resistance that increased with an increase in hold time at OCV (Figure 1.4). This behavior is likely a result of a chemical reaction between the electrolyte and the anode.

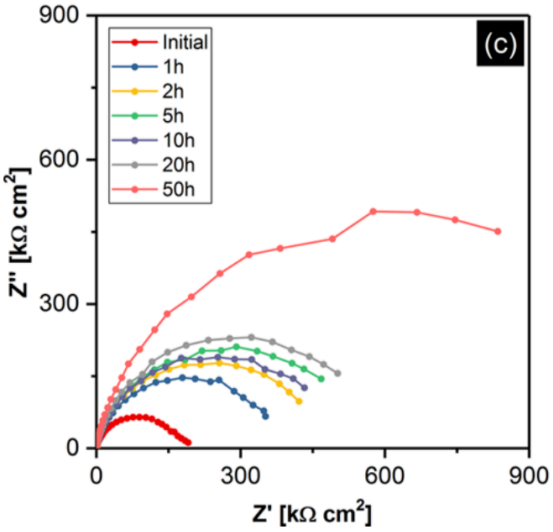

Figure 1.4 Nyquist plot of a Mg/Mg cell prior to electrochemical cycling. Interfacial resistance increases with an increase in hold time at OCV. Taken from Tutusaus *et al.*[15]

In work performed by Esbenshade *et al.*,[16] holding a Mg system at OCV led to an improvement in deposition overpotential, exchange current density, and Coulombic efficiency (CE). The authors attributed this result to the formation of a Mg-Cl "enhancement layer" on the anode surface. Taken together, these studies demonstrate that reactions occurring at the Mg anode/electrolyte interface are complex, and that understanding the processes governing surface reactivity would be helpful in improving electrolyte stability and extending cycle life. Likewise, it is important to clarify the role of additives, such as Cl, on these processes, given their apparent potential to improve electrochemical properties.

1.4 Lithium metal batteries

As with graphite anodes, lithium metal anodes exhibit a very negative redox potential (-3.04 V vs. standard hydrogen electrode) and are thus susceptible to electrochemical reaction with the electrolyte. Unfortunately, a stable SEI layer formed *in situ* in alkyl carbonate-based electrolytes does not occur for Li metal anodes.[17] Consequently, Li and electrolyte are both consumed in decomposition reactions, decreasing the CE, which measures the amount of Li ions available for plating and stripping in subsequent charge cycles. In addition, Li is not evenly plated and stripped on the anode. When Li is preferentially plated on the electrode, needle-like structures, termed dendrites, are formed. These dendrites increase in size until they eventually contact the cathode and short circuit the battery, leading to unwanted fires and explosions.

1.4.1 Protection strategies for lithium anodes

In order to achieve a more controlled SEI structure and to prevent the formation of dendrites, a number of artificial SEI materials have been considered for use as a protection layer at Li metal anodes. These include, but are not limited to, LiF,[18] Al_2O_3,[19–21] a polymer coating,[22–24] and carbon nanospheres.[25] Nonetheless, many of these materials are not well-suited for such an application. LiF and Al_2O_3, for instance, are poor ionic conductors.[26,27] Further, all of the characteristics necessary for a protective membrane often are not considered collectively. This membrane should promote high Li-ion conductivity, have high mechanical strength to suppress dendrite nucleation, block the direct interaction of the anode with the electrolyte to prevent electrolyte decomposition, and exhibit little to no electronic conductivity.

Two-dimensional (2D) structures are a promising class of materials for a protective membrane. Owing to their thin, yet rigid structure, 2D materials possess high Li-ion transport properties and mechanical integrity.[28] Further, certain 2D materials may also block electrolyte decomposition and electron transport. One particular 2D material, graphene oxide (GO), has gained attention as a physically blocking membrane that may exhibit all of these properties.[29–32] To the best of our knowledge, the utility of employing a GO membrane for Li anode protection remains underexplored in the modeling community.

1.4.2 Native oxide layer on lithium metal

Although the use of physical membranes for Li anode protection allows for improved control of the anode/electrolyte interface, it does not allow for complete control. One of the most underexplored aspects of the SEI is the native oxide layer on Li metal. Because Li metal is so reactive, it will virtually always have a native oxide layer present on its surface, even when fabricated in an oxygen-poor environment. Thus, when a Li foil electrode is implemented in a battery, the innermost SEI layer is the native oxide. Interestingly, many studies attribute the cycling behavior of lithium metal batteries to components that are found in the native oxide layer on the Li metal surface.[33–39] Nonetheless, to our knowledge, the role of the native oxide layer in the SEI has not been explicitly investigated.

Using X-ray photoelectron spectroscopy (XPS), experimentalists have characterized the structure of the native oxide layer.[40,41] In general, there is an inner layer of Li_2O and an outer layer of LiOH and Li_2CO_3. See Figure 1.5 for an illustration of the composition of the native oxide layer. Therefore, the innermost SEI layer in a battery employing a Li anode is expected to be Li_2O. Given

the large variance in SEI compositions in lithium metal batteries,[42] an improved understanding of the structure and Li-ion transport properties of this oxide layer would greatly benefit the battery community.

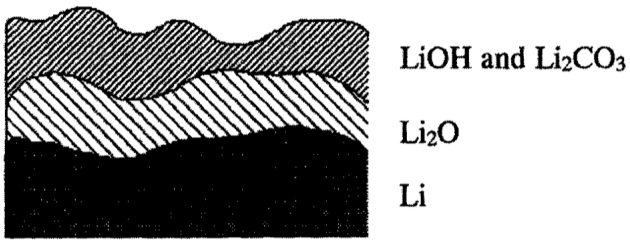

Figure 1.5 Inferred structure of the native oxide layer on lithium foil (as-received from a vendor) based on XPS results. Taken from Kanamura *et al.*[41]

1.5 Goals and outline of this dissertation

In line with the preceding discussion, the main goal of this dissertation is to use first-principles modeling to shed light on the atomistic factors governing the successful implementation of metallic anodes in next-generation batteries. This dissertation focuses on two battery architectures: Mg metal and Li metal batteries. In Chapter 2, the theoretical foundations for the main methodologies employed in this work are discussed.

Chapter 3 addresses one of the key challenges related to Mg metal batteries: electrolyte decomposition. This chapter examines the energetics of solvent decomposition on various Mg anode surface compositions. Density functional theory (DFT) calculations are performed to predict both the thermodynamic driving force (reaction enthalpy) and kinetics (activation energy) of plausible decomposition reactions on three Mg anode surface phases: Mg metal, MgO, and $MgCl_2$. Using Bader Charge analysis, reductive charge transfer from the metallic electrode is shown to minimize reaction barriers and stabilize decomposition products. The presence of an oxide or chloride surface film is predicted to hinder the charge transfer process, limiting solvent decomposition. The analysis in this section provides insight into the mechanisms by which the composition of the anode surface influences electrolyte decomposition.

In Chapters 4 and 5, the key challenges related to Li metal batteries are analyzed. Chapter 4 investigates aspects of a GO membrane as a protective layer for a Li metal anode. Specifically, the work of adhesion, an important mechanical property, is computed for multiple GO structures and the results are compared with other Li anode/electrolyte interfaces reported in the literature.

In Chapter 5, the native oxide layer on Li metal is modeled with a crystalline slab supercell structure and an amorphous oxidized slab model. In the latter scenario, a simulated oxidation algorithm using *ab initio* molecular dynamics (AIMD) is employed in which O_2 molecules are incrementally added to an initially pure Li slab until an amorphous oxide layer is grown. The oxidation algorithm is meant to more closely mimic the formation of the oxide layer in nature in order to provide a more realistic depiction of the anode/native oxide interface. The structure of the amorphous model is then characterized using radial distribution functions, charge transfer analysis, and differences in Li core-level electron binding energies. The results are compared with crystalline structures to quantify the progression of oxidation in the model. In addition, the transport properties of Li^+ through the oxide layer are assessed with AIMD.

Finally, Chapter 6 draws conclusions based on the analyses presented in the earlier chapters. Findings are presented in the context of batteries and important consequences for anode/electrolyte interfaces are enumerated. Future work is also suggested; if pursued, these efforts may provide answers to some of the open questions that remain.

Chapter 2: Methodology

2.1 Density functional theory

One of the main computational tools employed in this dissertation is DFT. In DFT, the ground state energies of atomic systems are computed from the electron density. Throughout this dissertation, DFT will be used to compute the lowest energy structures in various systems. The lowest energy structures of materials are typically the most interesting from a scientific point of view since they are the most likely configurations in which to find a system. In this section, the theoretical basis for DFT is presented.

In principle, in order to compute the energy of a collection of atoms, one would solve the Schrödinger equation (shown below in its time-independent form):

$$\left[-\frac{\hbar^2}{2m}\sum_{i=1}^{N}\nabla_i^2+\sum_{i=1}^{N}V(\mathbf{r}_i)+\sum_{i=1}^{N}\sum_{j<i}U(\mathbf{r}_i,\mathbf{r}_j)\right]\psi = E\psi \tag{2.1}$$

where m is the electron mass. The expression in brackets is the Hamiltonian of the system. From left to right, the terms correspond to the kinetic energy of the electrons, the potential between electrons and nuclei, and the interaction between electrons. Unfortunately, solutions to the Schrödinger equation are not practical for real systems since, for an N-electron system, the equation is a function of $3N$ coordinates.

In the 1960s, Kohn and Hohenberg developed an alternative approach for computing the energy of a collection of atoms. They recognized that "the ground-state energy from Schrödinger's equation is a unique functional of the electron density." [43] In other words, the dimensionality of the problem could be reduced from $3N$ dimensions to just 3 dimensions since the electron density is a function of only three spatial coordinates. The functional mentioned in the theorem is an expression that takes a function, the electron density $E[n(\boldsymbol{r})]$ in this case, and returns a value, the ground state energy. Further, based on a second theorem by Kohn and Hohenberg, it is possible to

fully solve the Schrödinger equation by determining the electron density that minimizes the total energy functional.[44]

The procedure for determining the electron density was subsequently laid out by Kohn and Sham in the Kohn-Sham equations, where the energy of a collection of atoms is expressed in terms of single-electron wave functions:[45]

$$\left[\frac{\hbar^2}{2m}\nabla_i^2 + V(\mathbf{r}) + V_H(\mathbf{r}) + V_{XC}(\mathbf{r})\right]\psi_i(\mathbf{r}) = \varepsilon_i\psi_i(\mathbf{r}) \tag{2.2}$$

The main difference between equations 2.1 and 2.2 is that the Hamiltonian has been recast from a summation over all electron wave functions to single-electron wave functions that depend on only three spatial coordinates. The first two terms in the Hamiltonian appeared in the Schrödinger equation (2.1). However, the other two terms require some explanation. $V_H(\mathbf{r})$ is the Hartree potential, and it describes the Coulomb repulsion felt by a single electron due to the total electron density. The electron density takes into account the contribution from all of the electrons in the system, including the specific electron being described in the Hartree potential. Therefore, there is an unphysical self-interaction term included in the Hartree potential. A correction for this unphysical behavior is included in the final term in the Hamiltonian, $V_{XC}(\mathbf{r})$, which accounts for the exchange and correlation contributions.

The exchange and correlation contributions are determined by an exchange-correlation functional, $E_{XC}(\mathbf{r})$. This functional is the only parameter that cannot be written down in an analytical form; thus, it must be approximated. A variety of exchange-correlation functionals have been developed in the literature. One of the most common is the Perdew-Burke-Ernzerhof (PBE) functional.[46] PBE uses the generalized gradient approximation (GGA), which takes into account both the local electron density and gradient of the density to approximate the exchange-correlation energy functional. The exchange-correlation functional used in each calculation presented in this dissertation will be noted in the text.

Upon closer examination of equation 2.2, it may be obvious that the electron density is required in order to solve the Kohn-Sham equations. Yet, these equations were also advertised as a procedure for determining the electron density. The solution to this conundrum is that DFT involves a self-consistent calculation of the ground state energy. A complete DFT calculation involves the following steps:

1. Define a trial electron density, $n(\boldsymbol{r})$.
2. Solve the Kohn-Sham equations with this electron density to compute the single-electron wave functions, $\psi_i(\boldsymbol{r})$.
3. Recompute the electron density from the computed single-electron wave functions in the previous step
4. Compare the computed electron density with the trial electron density. If the two values are equivalent, this is the ground state electron density. If not, update the trial electron density and repeat the procedure.
5. Compute the total energy from the ground state electron density.

2.2 Plane wave DFT

All of the DFT calculations presented in this dissertation are computed in the Vienna *ab initio* simulation package (VASP).[47–50] VASP uses periodic boundary conditions to represent systems, making it well-suited for solid-state materials. From Bloch's Theorem, in a periodic solid, the wave function for each electron can be written in terms of a modulating wave and a function having the same periodicity as the crystal lattice:[43]

$$\phi_k(\mathbf{r}) = \exp(i\mathbf{k}\cdot\mathbf{r})u_k(\mathbf{r}) \tag{2.3}$$

The first term on the right-hand side is the modulating wave and the second term is a function having the same periodicity as the lattice. This representation of the wave function is termed a plane wave. The accuracy of a DFT calculation can be systematically improved by including more plane waves in the basis set. Practically, the number of plane waves is determined by specifying an energy cutoff for the plane wave basis set.

In defining the expression for a plane wave in equation 2.3, a new vector, $\boldsymbol{k}$, has been introduced. This vector defines the positions of atoms in reciprocal space. As the name implies, the vectors $\boldsymbol{k}$ are the reciprocal of position vectors in real space, $\boldsymbol{r}$. The transformation of position vectors to $\boldsymbol{k}$-space allows for tractable solutions for periodic systems. The accuracy of a DFT calculation can also be improved by increasing the *k*-point grid. In the specific studies described later in this dissertation, values for the plane wave energy cutoff and *k*-point grid are explicitly listed.

Although plane waves are a convenient basis set for periodic systems, many plane waves are required to treat tightly-bound, core electrons. Therefore, a pseudopotential approximation that does not explicitly treat electrons in the core region is employed. Since the physical properties of materials, and of their reactivity, most strongly depend on the valence electrons, this type of approximation is still able to reproduce experimental behavior. Computations in this dissertation use a projector augmented wave (PAW) pseudopotential.[51,52]

2.3 Nudged elastic band method

In Chapter 3, the nudged elastic band (NEB) method is used to determine the reaction barriers for solvent decomposition on Mg anode surface compositions.[53] The NEB method allows one to calculate the minimum energy path (MEP) between two configurations. This is done by building a set of images of roughly equal spacing between the initial and final configurations and by minimizing the energy at each image. Images are constrained to be of roughly equal spacing between one another by a spring force that acts parallel to the MEP. The energy is minimized at each image by making the forces perpendicular to the path at each image go to zero. The energy barrier on the MEP is then used as an estimate for the activation barrier for a reaction.

2.4 Charge partitioning

The electron density from DFT can be used to not only compute the ground state energy of a system, but also to compute the charges on each atom. The charge on a given atom is determined by subtracting the local electron density from the valence charge density of the atom. For instance, if an O atom with a valence charge density of 6 e^- has a local electron density corresponding to 7.4 e^-, then the charge on the O atom would be -1.4. Different methods exist for determining how to partition the charges on each atom. In this dissertation, two approaches are used. The first, Bader partitioning, divides charge according to extrema in the charge density profile. The coordinates of an atom are defined by a maximum in the charge density and the dividing surface around an atom is set by minima in the charge density. All charge enclosed within the dividing surface around an atom is assigned to that atom. The other charge partitioning technique employed in this work is Voronoi partitioning. In the Voronoi partitioning scheme, charge is assigned to an atom within a geometrical region around that atom. This geometrical region is defined by Voronoi polyhedra.

2.5 Core-level binding energy shifts

The binding energy of a core electron, which is typically assessed with XPS, can also be calculated computationally and compared with experiment. This is performed by exciting an electron (or a partial electron) from the core to the valence or conduction band and computing the change in energy between the ground state and the excited state. Two equivalent methods for determining the binding energy are employed in this dissertation – the final state and transition state approaches.[54,55] In the final state approach, the binding energy is determined as a simple energy difference between the ground state (electron still in core state) and the excited state (core electron has been excited):

$$BE_i^{FS} = E(n_i - 1) - E(n_i) \tag{2.4}$$

where $E(n_i-1)$ is the energy of the system in the excited state and $E(n_i)$ is the energy of the system in the ground state. In the transition state approach, half an electron is moved from the core to the valence or conduction band and the negative of the eigenvalue of the excited core state is used to determine the core electron binding energy. In both approaches, valence electrons are allowed to relax after the electron excitation occurs, which results in a screening of the core hole. Since the calculation of absolute binding energies are not accurate in a ground state approach such as DFT, binding energy *shifts* are typically computed instead:

$$E_{CLS} = BE - BE^{ref} \tag{2.5}$$

where the binding energy is computed with respect to a reference system. In equation 2.5, the core-level shift (CLS) results in a more accurate comparison with experiment. To validate this approach, the Li 1s CLSs of various bulk materials containing Li were computed using the final state approach and compared with experiment (Figure 2.1). A minimum of seven experimental values were used for each material and the error in experimental values is reported as plus or minus the standard deviation. The binding energies were all referenced to Li_2CO_3 since that material had the least amount of experimental deviation. As evidenced in the figure, all computed values are very close to the experimental values, and only the computed value for LiOH falls outside of the experimental standard deviation. As such, this approach is expected to achieve good accuracy for the Li metal and Li_2O systems considered in this dissertation.

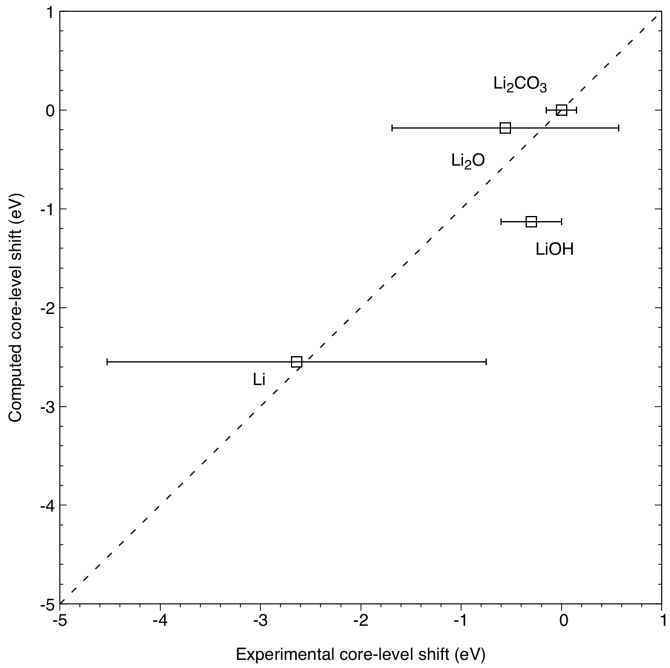

Figure 2.1 Comparison between computed Li 1s core-level binding energy shifts and experimental binding energy shifts relative to Li_2CO_3 for bulk compounds containing Li. CLSs were computed with the final state approach. The dashed line represents the line of perfect agreement between computation and experiment. Error bars display the standard deviation of the experimental data.[56–75]

2.6 *Ab initio* molecular dynamics

DFT is a very useful technique for computing the ground state energies of stationary systems. It's also possible to predict reaction mechanisms with DFT if we can reasonably determine the structure of the reactants and products. Nevertheless, in the real world, atoms are in constant motion and there are many scenarios where it is useful to be able to predict how the atoms in a system evolve with time. For example, in Chapter 5 we use AIMD to grow a realistic structural model of the interface between Li metal and its native oxide, and further employ dynamical simulations to compute the ionic transport of Li^+ in the model systems. In this section, the theory behind AIMD is described.

The main idea of molecular dynamics is to evolve a system of atoms forward in time by moving the atoms in that system in response to the forces on each atom. This is precisely what Newton's equations of motion say:

$$F_i = m_i a_i = m_i \frac{dv_i}{dt} \tag{2.6}$$

The force on a particular atom, F_i, causes that atom to move with an acceleration, a_i, in proportion to its mass, m_i. In MD, it is usually more convenient to write the acceleration as a time derivative of the velocity, as shown above. This is because one of the most important outputs of a MD calculation is the trajectory file, which is a list of the positions and velocities of all of the atoms as a function of time. The forces on each atom are determined from the potential energy, U, as:

$$F_i = \frac{\partial U}{\partial r_i} \tag{2.7}$$

This is where the two types of MD, classical and *ab initio*, differ. In classical MD, the potential energy is computed based on a user-specified force field. This force field includes bonded and non-bonded interactions between all atoms in the system and is typically parameterized for a system of interest. In AIMD, the potential energy is computed with DFT. Consequently, there is a tradeoff between accurate energy computation and simulation time. AIMD is able to more accurately compute the potential energy of a system than classical MD because it treats the electrons explicitly in the calculation, but it cannot simulate as long of timescales.

In classical MD, there are many interatomic potentials to describe the interactions between atoms. One of the most common, and simplest, is the Lennard-Jones potential (shown as a 12-6 type):

$$V_{LJ}(\mathbf{r}_{ij}) = 4\varepsilon_{ij}\left(\left(\frac{\sigma_{ij}}{r_{ij}}\right)^{12} - \left(\frac{\sigma_{ij}}{r_{ij}}\right)^{6}\right) \tag{2.8}$$

where ε_{ij} is the depth of the potential well and σ_{ij} is the distance at which the potential is zero. The general form of the Lennard-Jones potential is representative of various interatomic potentials. There is a large repulsive potential at short distances where atoms are very close to one another, an asymptotic trend towards zero potential when the atoms are far apart, and a mid-range distance at which the attractive potential is strongest, corresponding to a minimum on the potential surface. All of these features can be seen in Figure 2.2 below.

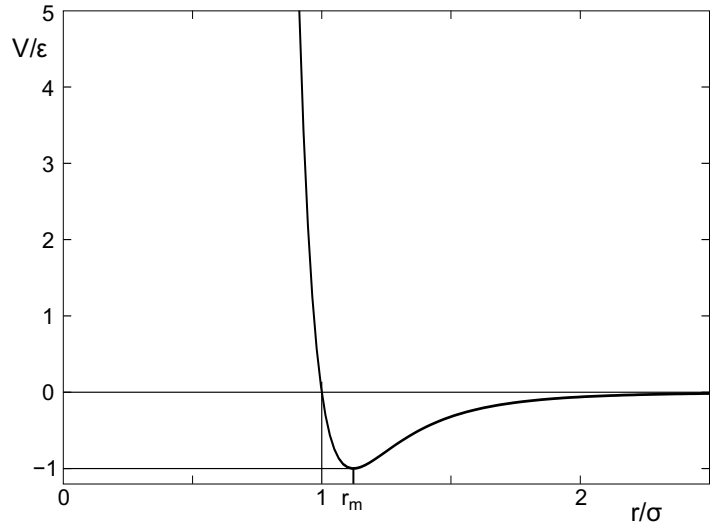

Figure 2.2 Lennard-Jones 12-6 potential.[76]

Using equations 2.6 and 2.7, it is now possible to write the general MD algorithm:

1. Input a system of atoms and specify the initial positions and velocities. For classical MD, bonded and non-bonded potential interactions must also be specified.
2. Evaluate equation 2.7 to compute the total force on each atom.
3. Solve equation 2.6 to compute the updated positions and velocities of all the atoms.
4. Move each atom accordingly and write the new positions and velocities to a trajectory file.
5. Repeat steps 2-4 until a user-specified number of time steps is reached.

In step 3, Newton's equations of motion must be integrated in order to obtain updated positions and velocities. Due to their complexity, they must be integrated numerically. A finite difference method is employed to do so. Among the simplest approaches is the Verlet algorithm. In this approach, the computation of positions is performed as:

$$x(t+\Delta t)=2x(t)-x(t-\Delta t)+\frac{d^2x}{dt^2}(\Delta t)^2+O(\Delta t^4) \tag{2.9}$$

In the above equation, both the previous time step and the current time step are used to compute the position in the next time step. The velocities are not explicitly given in equation 2.9, but they can be estimated using the position terms and the mean value theorem:

(2.10) $$v_x(t)= \frac{x(t+\Delta t)-x(t-\Delta t)}{2\Delta t}+O(\Delta t^2)$$

In order to perform an AIMD calculation, a thermodynamic ensemble must also be chosen. In other words, the user must specify which terms to be kept constant. In experimental systems, heat is typically exchanged with the surroundings to maintain a constant temperature and the number of particles typically does not change. Based on these factors, it is usually desirable to keep the number of particles (*N*) and the temperature (*T*) constant. It is then common for the last constant parameter to be either volume (*V*) or pressure (*P*). The choice of parameter is dictated by the system being studied. For the calculations presented in this dissertation, the NVT, or canonical ensemble, is used.

2.7 Mean-squared displacement and diffusion coefficients

Using AIMD trajectories, the mean-squared displacement (MSD) of atoms can be computed. In turn, the MSD can be used to compute the diffusion coefficient. The MSD is computed as the square of the atom displacement as:[77]

(2.11) $$MSD(\Delta t)=\frac{1}{N}\sum_{i=1}^{N}\frac{1}{N_{\Delta t}}\sum_{t=0}^{t_{tot}/2}|\mathbf{r_i}(t+\Delta t)-\mathbf{r_i}(t)|^2$$

where Δt is computed over all possible time origins, N is the number of atoms, $N_{\Delta t}$ is the total number of time intervals of length Δt used in the averaging, t_{tot} is the total simulation time, and the squared quantity is the squared atom displacement. Then, using the MSD, the Einstein relation allows one to compute the diffusion coefficient:

(2.12) $$D \propto \frac{MSD(\Delta t)}{2d\Delta t}$$

where d is the dimension of the system (d = 3 in this case). Basically, the slope of the line of best fit to the MSD curve is used to calculate the diffusion coefficient. However, only the diffusional displacement regime is used when fitting this line since this is the regime we care about. This regime generally corresponds to larger time intervals, and it can be distinguished from the

vibrational motion regime (at short time intervals) based on the shape of the MSD curve. In the vibrational motion regime, the MSD is proportional to $\Delta t^{1.42}$ as opposed to Δt for the diffusional displacement regime.

Chapter 3: Reaction pathways for solvent decomposition on magnesium anodes

3.1 Introduction

Section 1.3 highlighted one the challenges associated with magnesium metal batteries. This challenge is the formation of a passivation layer on the anode that blocks the transport of Mg^{2+} across the electrode− electrolyte interface.[1,8,78] It has been suggested that this passivation layer forms from the degradation of salt or solvent species present in the electrolyte.[1,7,8] Hence, many studies have focused on developing salts/solvents that circumvent this limitation and can reversibly plate and strip Mg at the negative electrode.[8–13] For example, ethereal solvents, such as THF and various glymes, have been demonstrated to be amongst the most successful at supporting reversible plating and stripping of Mg.[8,12]

Additional improvements in the plating and stripping behavior are desired, however, even in electrolytes composed of these solvents. For example, recent experimental studies have highlighted variability in the electrochemical behavior after holding ethereal solvent-based cells at OCV.[9,14–16] Tutusaus *et al*.[15] measured the voltage profile and cell resistance using symmetrical Mg/Mg cells for a monocarborane/tetraglyme-based electrolyte, which was recently reported to provide superior Mg plating and stripping performance.[12] Nevertheless, increased polarization and higher interfacial resistance were observed following a hold at OCV. Moreover, the interfacial resistance increased with the increasing hold time. These observations suggested the presence of a chemical reaction, such as electrolyte decomposition, occurring at the interface between the electrolyte and the Mg anode.

In other studies, a hold at OCV was found to be detrimental to Mg plating/stripping, similar to the work of Tutusaus *et al*., but the authors attributed the results to processes other than electrolyte decomposition on the anode surface. Barile *et al*.[9] observed an increase in deposition overpotential, a decreased stripping peak height, and a decrease in CE after a 1 week pause in cycling of the MACC/THF system. The decrease in the performance was ascribed to the formation of THF oligomers through ring-opening reactions that appeared to be catalyzed by the $AlCl_3$ in the MACC

solution. Connell *et al.*[14] reported a decrease in CE with an increase in the OCV hold time for the $MgTFSI_2$/diglyme system, which was related to surface passivation by trace amounts of H_2O.

Despite the findings described above, holding a system at open circuit is not always detrimental to the electrochemical behavior. Esbenshade *et al.*[16] cycled Mg electrodes in $PhMgCl/AlCl_3$ in THF and EtMgCl in diglyme. They found an improvement in deposition overpotential, exchange current density, and CE following a pause in cycling at open circuit. The authors attributed this behavior to the formation of a Mg− Cl enhancement layer on the anode surface.

Similarly, Connell *et al.*[14] found that the presence of Cl on the anode surface inhibited passivation. These authors proposed that surface-adsorbed Cl species may prevent salt decomposition, by blocking the interaction of the salt with Mg surface sites. Other work has shown similar results when Cl is present in the electrolyte.[10,79–81] For example, in the $Mg(TFSI)_2$/THF electrolyte examined by Sa *et al.*, chloride was reported to be a necessary additive to obtain reversible plating/ stripping.[80] By extension, one may hypothesize that the presence of Cl ions on the anode surface may also block solvent decomposition, resulting in improvements to the plating/stripping performance.

Taken together, these studies demonstrate that reactions occurring at the Mg anode/electrolyte interface are complex. Nevertheless, understanding the processes governing surface reactivity/passivation would be helpful in improving the electrolyte stability and extending the cycle life. Likewise, it is important to clarify the role of additives, such as Cl, on these processes, given their apparent potential to minimize anode passivation.

In an attempt to clarify the complex behavior at Mg anode/electrolyte interfaces, this chapter examines the energetics of solvent decomposition on various Mg anode surfaces with van der Waals-augmented density functional theory (vdW-DFT). Negative electrodes based on metallic magnesium, and on the surface phases expected to be present on those electrodes (MgO and $MgCl_2$) because of reactions with air or an electrolyte, are the focus of the present chapter. Our approach explores dozens of candidate chemical reactions on these surfaces during a hold at OCV. It also builds on previous studies,[82,83] wherein the electrochemical stability of several common solvents at interfaces with model Mg and oxide electrodes[3] was assessed and ion agglomeration in Mg electrolytes was examined.[84]

Here, surface decomposition reactions involving dimethoxyethane (DME) are explored across a set of model electrode surface compositions: Mg, MgO, and $MgCl_2$. The selected surface phases represent plausible compositions for a Mg anode. Similarly, DME was chosen as a prototype

solvent, given its common use in Mg batteries and its relatively simple structure.[1,9,85] A classical Monte Carlo (MC) algorithm coupled with vdW-DFT calculations was used to determine low-energy configurations for adsorbed (intact) DME. Subsequently, low-energy configurations for decomposed DME were identified on each surface. The thermodynamic and kinetic likelihood for solvent decomposition was assessed by computing reaction enthalpies and kinetic barriers between the intact and decomposed configurations.

These calculations suggest that the greatest likelihood for solvent decomposition occurs on the pristine Mg(0001) surface. Mg(0001) exhibits both a large (exothermic) thermodynamic driving force and a small kinetic barrier for solvent decomposition. The most likely decomposition products are adsorbed methoxy fragments and ethylene gas. The favorable energetics for this reaction are aided by reductive charge transfer from the electrode, which minimizes the reaction barriers and stabilizes decomposition products.

Conversely, the oxide and chloride surfaces are relatively inert. In these cases, the solvent decomposition reaction is roughly thermoneutral and furthermore, is characterized by very large kinetic barriers. The stability of the Cl-based surface may explain how Cl additions to an electrolyte contribute to improvements in the anode performance via a Mg−Cl enhancement layer. In total, this chapter provides insights into the mechanisms by which the composition of the anode surface influences electrolyte decomposition.

3.2 Methodology

DFT calculations were performed using VASP.[47–50] The exchange−correlation energy was determined using the functional of Perdew, Burke, and Ernzerhof,[46] coupled with the fully self-consistent vdW-DF2[86–89] functional to account for dispersion interactions between the solvent adsorbate and the electrode surface. Dispersion interactions were also necessary to accurately reproduce surface structures and surface energies. Most notably, in the absence of dispersion interactions, the energy of a $MgCl_2$(0001) slab is essentially equivalent to the bulk energy of $MgCl_2$. This is not a physically realistic scenario because it implies that there is no energy cost for forming a surface.[90] This discrepancy is avoided with the use of the vdW-DF2 functional.

Electronic wavefunctions were expanded in a plane wave basis, with a 400 eV energy cutoff, and the projector-augmented wave method was used to describe interactions between core and valence electrons.[51,52] Unless otherwise stated, the ions in each computational cell were allowed to relax until all forces were less than 0.04 eV/Å.

Each DME/surface computational cell was constructed to minimize the interaction with its periodic images. The vacuum region of the cell, which separated the adsorbed DME molecule and the bottom layers of the surface, was always greater than 10 Å. Computations were performed on the lowest energy surface for each model electrode composition. For pristine Mg, this was the (0001) termination, as shown in the literature,[91,92] and was confirmed by our own calculations. The computational cell for the DME/Mg system consisted of a 3 × 4 supercell with physical dimensions of 16.58 Å × 12.77 Å within the surface plane. The cell consisted of 112 atoms (including the DME molecule) and four surface layers, with the two bottom layers fixed at their bulk spacing. The k-point mesh was set to 2 × 2 × 1. For MgO and $MgCl_2$, the (100) and (0001) surfaces, respectively, were adopted as the lowest energy terminations, consistent with our previous study,[93] and with literature reports.[90,94] The DME/MgO ($MgCl_2$) system was expanded in a 4 × 4 (2 × 4) supercell with dimensions of 11.98 Å × 11.98 Å (12.83 Å × 14.82 Å). The resulting 144 (112) atom cell was four (six) layers thick, and the two (three) bottom layers were fixed to their bulk-like spacing. The k-point mesh for these insulating systems was set to 1 × 1 × 1. The minimum vacuum space between periodic images in the intact and decomposed configurations on each of the surfaces is, respectively, Mg: 8.7 Å and 8.0 Å; MgO: 6.1 Å and 6.0 Å; and $MgCl_2$: 7.4 Å and 6.9 Å.

The adsorption energy, E_{ad}, for DME on each surface was calculated as:

$$E_{ad} = E_{surf+DME} - E_{surf} - E_{DME} \quad (3.1)$$

where $E_{surf+DME}$ is the total energy of the adsorbed DME/surface system, E_{surf} is the energy of the isolated surface slab, and E_{DME} is the energy of the isolated DME molecule. The energy of the isolated molecule was evaluated in both gas and liquid phases. Although DFT adsorption energies are typically only calculated with respect to a gas-phase molecule, the liquid phase reference is more physically realistic in this scenario because the DME will be a liquid in a real battery. The energy of the liquid phase was determined by subtracting the experimental latent heat of vaporization (36 kJ/mol)[95] from the DFT gas-phase energy.

The adsorption of DME on a single side of the electrode surface will result in a dipole within the computational cell when periodic boundary conditions are applied. Such a dipole can, in principle, impact the energy and forces of the calculation in an unphysical fashion.[96] We determined the impact of dipole interactions in each DME/surface cell and found only a modest

effect; adsorption energies differed by, at most, around 3%. In addition, the effect of increasing the plane wave energy cutoff and the k-point mesh in each system was calculated. Again, the system energies displayed only modest differences, with the largest effect modifying the adsorption energy by around 10%.

Our calculations assume that DME decomposition occurs following adsorption of an intact DME molecule on the anode surface. A classical MC-simulated annealing algorithm and physical intuition were used to produce a set of low energy, intact adsorption configurations on each anode surface composition. Input to the MC algorithm included partial charges, which we calculated within DFT using the Bader charge analysis scheme;[97–100] a DFT-relaxed, fixed surface structure; a set of more than 200 low-energy conformations of the DME molecule; and the COMPASS II force field.[101] The five lowest energy configurations for each surface from the MC calculations were used as input to relaxation calculations using vdW-DFT.

In addition to these MC-generated structures, additional candidate structures were generated using the five main DME conformers found in the liquid state.[102] Intuition was used to position these conformers in a diverse set of positions on the anode surface, followed by relaxation with vdW-DFT. The results from both methods were analyzed, and the lowest energy adsorbed geometry for each surface structure was selected for further analysis. These adsorbed geometries will henceforth be referred to as "intact" configurations.

Starting from the intact configurations, the most probable decomposed structures were determined by calculating the energies of dozens of possible DME decomposition products on each surface. A single bond was systematically cleaved from the set of all possible bonds in the DME molecule (C–H, C–O, and C–C), and the fragmented molecule was placed at a distinct surface site and relaxed. All distinct surface sites were explored, and the fragmented molecule was rotated in both in-plane and out-of-plane directions so as to maximize the interaction with the surface. Cases in which two bonds were sequentially broken were also explored; in these situations, the relaxed structure following the first cleavage was used as the input for the second bond cleavage. In total, 190 decomposed configurations were investigated across all the surfaces.

Subsequently, the lowest energy, decomposed geometries were selected for further analysis. The NEB method was used to calculate the MEP between the intact and decomposed configuration on each surface. Each NEB calculation was performed using the Gamma point ($1 \times 1 \times 1$ k-point mesh) and with five images. Starting configurations for the images were determined by linear interpolation between the initial (intact) and final (decomposed) states. Additional spot check

calculations were preformed using a higher k-point mesh (2 × 2 × 1). In these cases, the NEB barriers showed only a moderate change; the largest difference from the Gamma point results was 0.08 eV.

Metadynamics[103–106] was also used to examine decomposition reactions on the Mg(0001) surface. Here, a bias potential in the form of Gaussian-shaped hills was deposited to the C–O bond in DME closest to the Mg surface. The bias potential had a height of 0.025 eV, a width of 0.025 Å, a deposition stride of 25 time steps, and a time step of 1 fs. The bias was applied to the C–O bond, as this was the first bond to break on the MEP, as determined by the NEB method. Before starting the metadynamics simulation, a short (0.32 ps) NVT molecular dynamics equilibration was carried out at a temperature of 300 K.

The impact of charge transfer on stabilizing reaction products on each surface was evaluated using a Bader charge analysis.[97–100] In the Bader approach, charges are calculated from the ground-state electron density; the coordinates of an atom are defined by a maximum in the charge density and the charge around that atom is assigned to it. Distinct atoms are identified by minima in the charge density. Charge transfer during a given decomposition reaction was monitored by evaluating the Bader charge on each atom as a function of distance along the MEP.

3.3 Results and discussion

3.3.1 Thermodynamics of DME decomposition

Figure 3.1 illustrates the structures of the three model Mg anode surfaces and of the solvent molecule (DME) investigated in this study. The surfaces, which include Mg(0001), MgO(100), and $MgCl_2$(0001), represent the lowest energy surfaces for each composition. In the case of $MgCl_2$, the Cl-terminated surface of α-$MgCl_2$ was selected. This surface was reported to be nearly three times lower in energy than the next lowest energy termination.[90] The DFT-computed surface energies as determined in the current study are 0.56, 0.83, and 0.10 J/m^2, respectively. These values compare favorably with the surface energies determined from similar calculations in the literature: 0.55,[91] 0.88,[93] and 0.097 J/m^2,[90] respectively. The most favorable DME adsorption geometries on each surface, representing the intact configurations, are shown in Figure 3.2. The corresponding DFT adsorption energies with respect to liquid phase DME are given in Table 3.1.

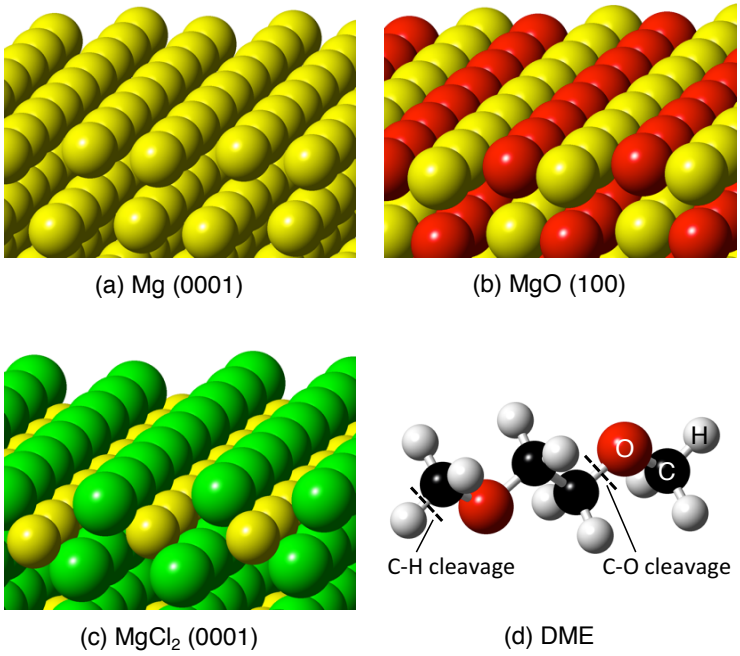

Figure 3.1 Model magnesium anode surface compositions examined in this study: (a) Mg(0001), (b) MgO(100), and (c) Cl-terminated $MgCl_2$(0001). (d) Structure of the solvent, DME, examined in this study. Sample cleavage points for C–H and C–O bonds are shown. Mg, O, Cl, C, and H atoms are colored yellow, red, green, black, and white, respectively.

DME adsorbs exothermically (corresponding to a negative adsorption energy in equation 3.1) on all surfaces. However, adsorption is more exothermic on the Mg and MgO surfaces, with energies of −0.32 and −0.52 eV, respectively, compared with −0.02 eV on $MgCl_2$. Mg atoms can be found in the surface layer for both Mg and MgO slabs, and on these surfaces, adsorbed DME orients itself so that the ethereal O atoms in DME are directly above these Mg atoms. Figure 3.2a,b shows that adsorbed DME adopts a bent geometry on these two surfaces, which is distinct from the linear geometry observed for isolated DME. The distances between surface Mg and O within DME are 2.40 and 2.25 Å on Mg(0001) and 2.46 and 2.25 Å on MgO(100). These distances are slightly larger than the Mg–O bond distance in bulk MgO of 2.11 Å. On $MgCl_2$, DME maintains the lowest energy (roughly linear) conformation, Figure 3.2c,f, observed for an isolated molecule,[102] consistent with a weak interaction with the surface and its nearly thermoneutral adsorption energy.

Table 3.1 Summary of calculated adsorption (ΔE_{ad}), reaction (ΔE_{rxn}), and activation (E_a) energies on each model anode surface. ΔE_{ad} is the adsorption energy for DME with respect to the liquid phase (eq 3.1), ΔE_{rxn} is the reaction energy associated with the decomposition of DME (eqs 3.2–3.4), and E_a is the activation energy for the decomposition reaction.

Surface	ΔE_{ad} (eV)	ΔE_{rxn} (eV)	E_a (eV)
Mg (0001)	-0.32	-4.04	0.24
MgO (100)	-0.52	-0.03	2.92
$MgCl_2$ (0001)	-0.02	-0.06	3.52

As explained in the previous section, the energies of dozens of decomposed DME configurations (63 on Mg, 74 on MgO, and 53 on $MgCl_2$) on each surface were calculated by cleaving a C–H, C–O or C–C bond. In some cases, a second bond was also cleaved. An earlier study on the $LiMn_2O_4$ surface found that cleaving a second bond was necessary to arrive at a low-energy decomposed structure.[83]

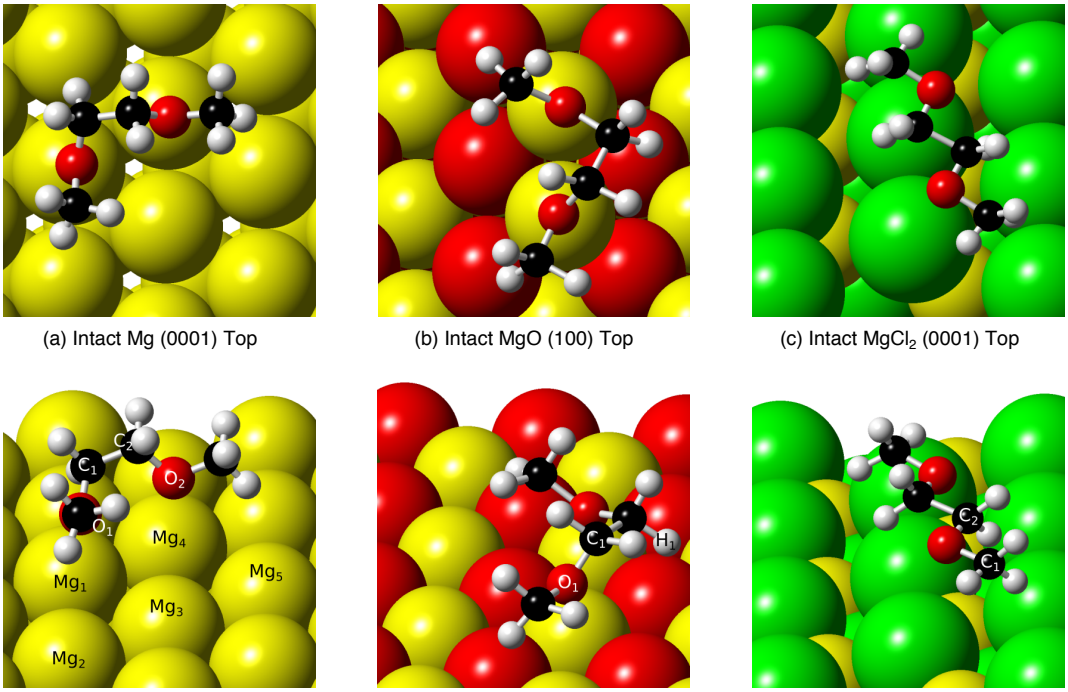

(a) Intact Mg (0001) Top (b) Intact MgO (100) Top (c) Intact $MgCl_2$ (0001) Top

(d) Intact Mg (0001) Side (e) Intact MgO (100) Side (f) Intact $MgCl_2$ (0001) Side

Figure 3.2 Images of the lowest energy intact configurations of DME on: (a,d) Mg(0001), (b,e) MgO(100), and (c,f) Cl-terminated $MgCl_2$(0001).

Figure 3.3 shows a summary of the DFT-calculated decomposition energies with respect to the intact configuration on each surface (structures that relaxed back to the intact configuration following bond cleavage have been omitted). Turning first to Mg(0001), Figure 3.3a, the

calculations reveal that DME decomposition is strongly exothermic on this surface: there exist many decomposed configurations that are more than 1 eV lower in energy than the intact configuration. Furthermore, we observe that bond cleavages that create larger molecular fragments tend to be favored over the abstraction of smaller molecules (or atoms). For example, the abstraction of a methoxy (CH_3O) fragment is energetically preferred over the abstraction of an H atom by roughly 2 eV. This is explained by the fact that these larger fragments tend to be electron-deficient, yet they can compensate for this deficiency by pulling electron density from the pristine Mg surface (as shown below).

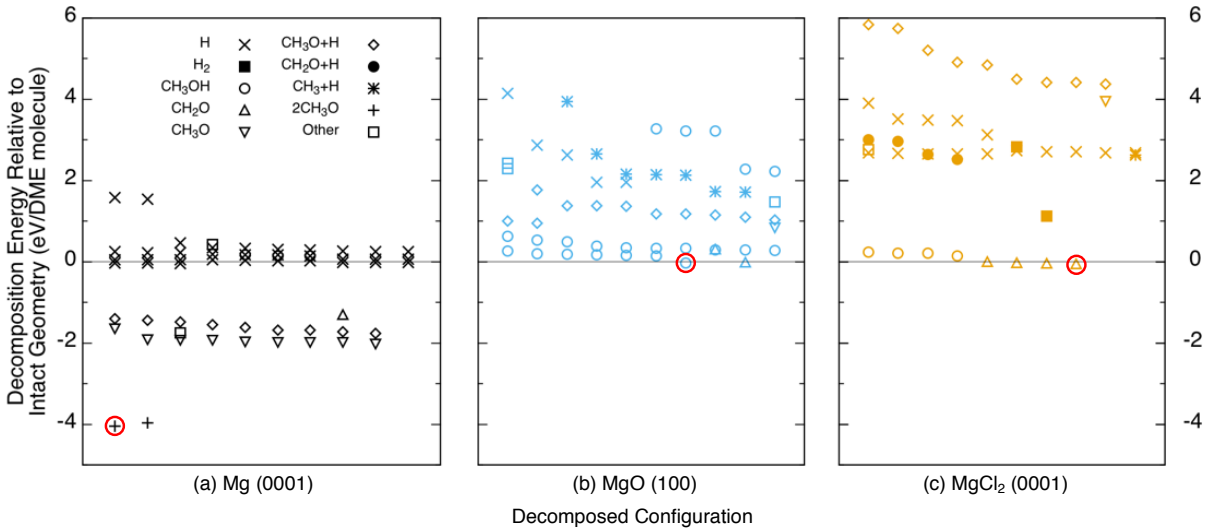

Figure 3.3 Energies of various DME decomposition products with respect to intact, adsorbed DME on the (a) Mg, (b) MgO, and (c) $MgCl_2$ surfaces. Negative energies represent an exothermic decomposition reaction. The symbol shape identifies the different types of decomposition products. The lowest energy products are circled in red and are depicted in Figure 3.4.

In contrast, DME decomposition is approximately thermoneutral on the MgO and $MgCl_2$ surfaces, Figure 3.3b,c: more specifically, the decomposed configurations (circled in red) on MgO or $MgCl_2$ are only slightly lower in energy (less than 0.1 eV) than the intact configuration. Nonetheless, the presence of the oxide and chloride surfaces do have a small but favorable energetic effect, as they reduce the decomposition energies relative to their values in the gas phase. For example, these gas-phase decomposition energies (determined from a difference in the energies of intact and decomposed DME, using the same decomposition products as found for the surface-mediated reaction) are endothermic: 0.25 eV (assuming MgO products) and 0.04 eV (assuming $MgCl_2$ products) for MgO and $MgCl_2$, respectively. In general, the most favorable

decomposition products on these surfaces are stable molecules (i.e., satisfying the octet rule) that exhibit negligible charge transfer with the surface (as will be shown below).

The energies of the most favorable decomposition reactions, ΔE_{rxn}, are shown in Table 3.1. These data demonstrate that DME decomposition is thermodynamically favorable on the pristine Mg surface; here, decomposition is strongly exothermic, $\Delta E_{rxn} = -4.04$ eV, with respect to the intact structure. There is little-to-no thermodynamic driving force, however, for DME decomposition on the oxide and chloride surfaces, $\Delta E_{rxn} = -0.03$ and -0.06 eV, respectively. As will be shown later, these reaction energies can be correlated with the ability of the pristine Mg surface to stabilize the DME decomposition products via charge transfer.

The most favorable decomposed configurations on each surface were subjected to additional analysis. The geometries of these configurations are depicted in Figure 3.4. On Mg(0001), the lowest energy decomposed configuration can be obtained from the intact structure via the cleavage of two C–O bonds, forming two CH_3O (methoxy) fragments that dissociate from the DME molecule and move to hollow hcp sites on the surface. NEB calculations (discussed below) indicate that the methoxy fragments break off from the original DME molecule sequentially. Following the abstraction of the methoxy fragments, the remainder of the DME molecule evolves from the surface as ethylene gas (C_2H_4). Thus, the overall reaction is given by:

$$C_4H_{10}O_2 \rightarrow 2CH_3O + C_2H_4(g) \tag{3.2}$$

where $C_4H_{10}O_2$ is the intact, adsorbed DME, $2CH_3O$ represents the two adsorbed methoxy fragments, and C_2H_4 is a gaseous ethylene molecule. Ethylene gas has been reported to evolve in Li battery cells in both EC-based electrolytes[107,108] and in DOL/DME-based solutions.[109]

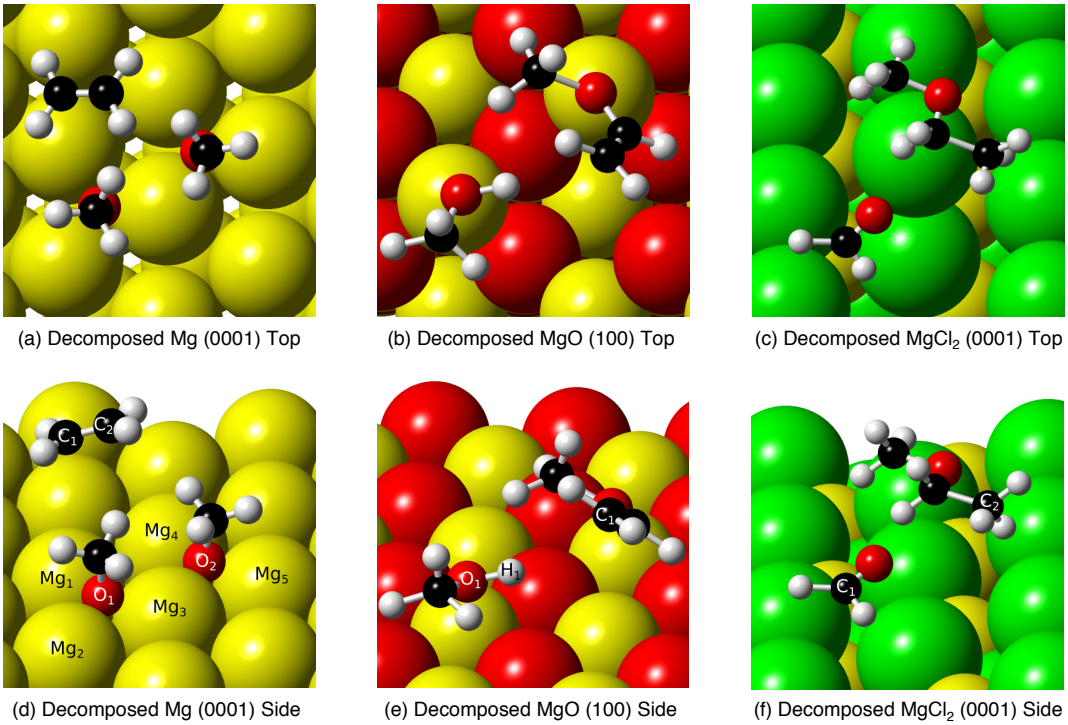

Figure 3.4 Lowest energy decomposition products of DME on (a,d) Mg(0001), (b,e) MgO(100), and (c,f) $MgCl_2$(0001).

On the MgO and $MgCl_2$ surfaces, the most stable decomposed configurations are formed through a single C–O bond cleavage, in conjunction with the exchange of an H atom between the two fragments formed by this cleavage. The overall reaction on MgO is:

(3.3) $$C_4H_{10}O_2 \rightarrow CH_3OH + CH_2CHOCH_3$$

and on $MgCl_2$, the overall reaction is:

(3.4) $$C_4H_{10}O_2 \rightarrow CH_2O + CH_3CH_2OCH_3$$

where CH_3OH, CH_2CHOCH_3, CH_2O, and $CH_3CH_2OCH_3$ represent DME fragments that remain adsorbed to the surface following decomposition.

On both MgO and $MgCl_2$, the initial C–O bond cleavage creates two species on the surface: a methoxy fragment and the remainder of the DME molecule. On MgO, a H atom is transferred from the remaining DME fragment to the methoxy fragment, generating a methanol (CH_3OH) and a methyl vinyl ether (CH_2CHOCH_3) molecule. It was postulated in a recent experimental study that

methanol was formed as an intermediate product in the decomposition of a diglyme-based electrolyte in a lithium–sulfur battery.[110] On $MgCl_2$, H atom transfer between fragments is also observed but occurs in the opposite direction. That is, H is transferred from the methoxy fragment to the remaining DME fragment, leaving a formaldehyde (CH_2O) and a methyl ethyl ether ($CH_3CH_2OCH_3$) molecule on the surface.

3.3.2 Reaction barriers for DME decomposition

Following the analysis of the thermodynamic viability of DME decomposition on each surface, the kinetics of the three primary decomposition reactions were subsequently assessed. This was accomplished by determining the reaction barriers from NEB calculations. The MEPs (calculated from the NEB) for the decomposition reactions are shown in Figure 3.5; the heights of the corresponding reaction barriers are listed in Table 3.1. Images showing the instantaneous structure of the DME/surface systems along the MEP are shown as insets in Figure 3.5. The initial and final points on each curve correspond to the intact (Figure 3.2) and decomposed (Figure 3.4) configurations, respectively. All energies are plotted with respect to the intact configuration, which is assigned an energy of zero.

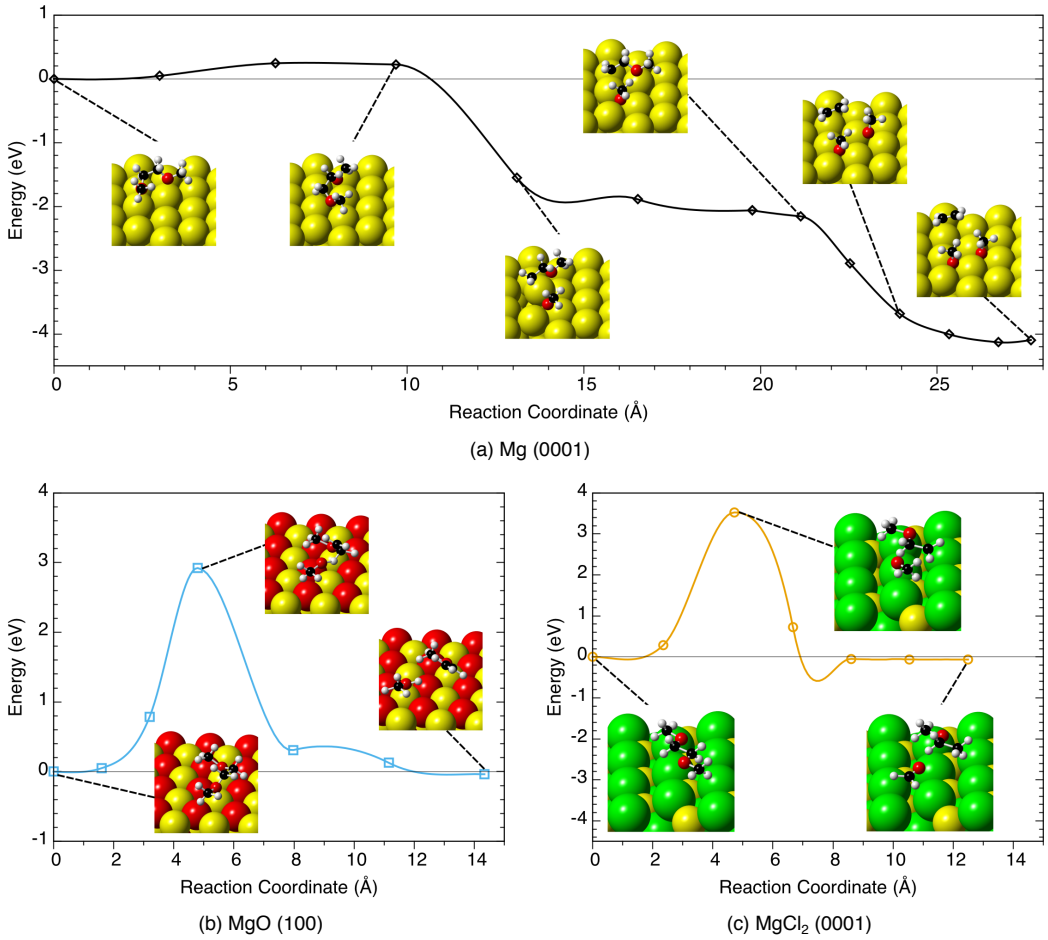

Figure 3.5 Minimum energy pathways for the most favorable DME decomposition reactions on (a) Mg(0001), (b) MgO(100), and (c) $MgCl_2$(0001) obtained using the NEB method. Energies are with respect to the intact, adsorbed configuration on each surface, corresponding to the point at which the reaction coordinate is equal to zero.

Turning first to the pristine Mg surface, Figure 3.5a shows that the MEP exhibits two downhill steps in energy, corresponding to two C–O bond cleavages. The barrier for the first bond cleavage is relatively small, 0.24 eV, whereas the second bond cleaves spontaneously (i.e., without a barrier). The low kinetic barrier for this pathway suggests that DME decomposition should be a rapid process on the pristine Mg surface.

In contrast, on the MgO and $MgCl_2$ surfaces, the MEP in both cases exhibits a single, very large barrier with heights of 2.92 and 3.52 eV, respectively, Figure 3.5b,c. Earlier, we described DME decomposition on these surfaces as occurring through a combination of C–O bond cleavage and H exchange between fragments. The NEB calculations indicate that the barrier associated with these reactions can be primarily attributed to the H-exchange step, with C–O cleavage occurring before the maximum on the MEP is reached. These large barriers suggest that DME decomposition

is kinetically hindered on the oxide and chloride surfaces. (We note the existence of a dip on the $MgCl_2$ MEP, Figure 3.5c, between the third and fourth images, suggesting that there is a configuration with a lower energy than the decomposed state. However, this appears to be an artifact of noisy forces; adding a new image between the original third and fourth images and re-running the NEB did not converge to a configuration lower in energy than the decomposed state.)

The mechanism for DME decomposition on the pristine Mg surface was also evaluated using an approximate metadynamics[103–106] simulation at 300 K. This simulation is described as "approximate" because relatively large bias-potential depositions were applied at a rapid rate, to minimize the computational expense. The reaction barrier can be overestimated under these conditions. Nevertheless, the metadynamics simulations predicted a reaction mechanism that was nearly identical to that obtained with the NEB, including the cleavage of the second C–O bond without the application of a bias potential. This observation lends further support for the spontaneous abstraction of the second methoxy fragment, consistent with the NEB results. As expected, the free-energy barrier via metadynamics, 0.58 eV, is larger than that obtained from the NEB. While some portion of the larger barrier may be traced to entropic effects, we also anticipate that smaller increments to the bias potential and more time between bias-potential depositions will also yield a barrier more similar to that of the NEB, as previously mentioned.

3.3.3 Charge-transfer analysis

Charge transfer between DME and each anode surface was analyzed using a Bader charge analysis. [97–100] The evolution of the Bader charges along the MEP on each surface is displayed in Figure 3.6 and summarized in Table 3.2. For clarity, we have limited our discussion to only those atoms showing an appreciable change in their Bader charge between the intact and decomposed states.

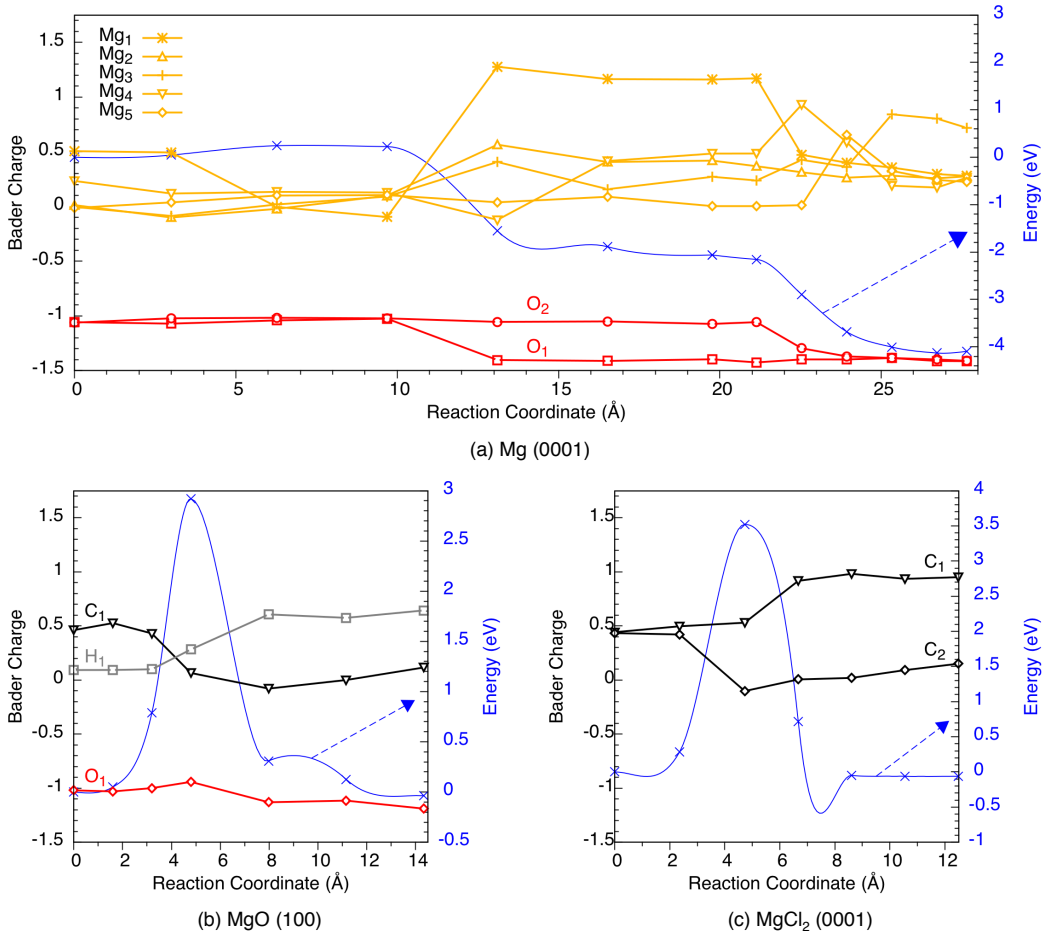

Figure 3.6 Evolution of Bader charge on selected atoms as a function of the reaction coordinate for DME decomposition on: (a) Mg, (b) MgO, and (c) $MgCl_2$ surfaces. For clarity, only those atoms exhibiting significant charge transfer are shown. Atoms are labeled using the same scheme as in Figures 3.2 and 3.4.

Bonding in the pristine Mg surface is metallic, whereas both of the MgO and $MgCl_2$ surfaces exhibit an ionic behavior. Consequently, electrons on the two ionic surfaces will be more localized than those in metallic Mg. This metallic behavior, and the fact that Mg is a relatively electropositive element,[111] suggests that the Mg surface is more amenable to oxidation than either of the more stable compounds, MgO or $MgCl_2$. This, in turn, allows for more facile donation of electrons to DME decomposition products, with the potential to stabilize these fragments.

During DME decomposition on the Mg surface, a total of 1.62 e^- is transferred from the surface to the decomposition products, Table 3.2. Figure 3.6a shows that there are two primary charge exchange events during the reaction, each coinciding with a downhill step in energy on the MEP and to a C–O bond cleavage. These charge exchanges occur at reaction coordinates of roughly 10 and 21 Å in Figure 3.6a. In both exchanges, charge is pulled from surface Mg atoms surrounding

the electron-deficient O atom in the recently abstracted CH_3O fragment. The relevant atoms are Mg_1, Mg_2, Mg_3, and O_1 in the first charge exchange, and Mg_3, Mg_4, Mg_5, and O_2 in the second exchange. As these charge-transfer processes coincide with decreases in energy, it appears that the transfer of charge stabilizes the decomposition products. In total, O_1 and O_2 are both reduced during DME decomposition, with each atom gaining 0.35 e–. On the other hand, the majority of surface Mg atoms ($Mg_{2–5}$) are oxidized; only Mg_1 experiences a net gain in charge, and it's charge state exhibits a complex fluctuation as a function of the reaction coordinate, Figure 3.6. The 0.24 electrons transferred to the intact DME (Table 3.2) is likely an artifact of inaccurate charge partitioning in the Bader analysis. In an earlier study (ref 3), it was determined that the lowest unoccupied molecular orbital (LUMO) for DME is 600 mV (GGA) to ~2 V (G_0W_0) more negative (i.e., higher in energy) than the Mg/Mg^{2+} level. This implies that the amount of charge transferred from the Mg electrode to the DME LUMO is negligible. The partial density of states for isolated DME and for selected adsorbed configurations along the decomposition reaction pathways on all three surface phases were also measured. The DME LUMO is positioned at a higher energy than the Fermi level of the surfaces, indicating that reductive charge transfer to intact DME is unlikely.

Table 3.2 Bader charges (in electrons) on selected atoms or on the entire DME molecule before (q_{intact}) and after ($q_{decomposed}$) DME decomposition. Δq is the net charge transferred during DME decomposition ($\Delta q = q_{decomposed} - q_{intact}$).

Mg (0001)	q_{intact}	$q_{decomposed}$	**Δq**
Mg_1	0.51	0.28	-0.23
Mg_2	0.01	0.28	0.27
Mg_3	0	0.72	0.72
Mg_4	0.23	0.26	0.03
Mg_5	-0.01	0.22	0.23
O_1	-1.06	-1.41	-0.35
O_2	-1.06	-1.41	-0.35
DME molecule	-0.24	-1.86	-1.62
MgO (100)	q_{intact}	$q_{decomposed}$	**Δq**
C_1	0.46	0.12	-0.34
H_1	0.09	0.64	0.55
O_1	-1.02	-1.19	-0.17
DME molecule	-0.08	-0.08	0
$MgCl_2$ (0001)	q_{intact}	$q_{decomposed}$	**Δq**
C_1	0.44	0.95	0.51
C_2	0.43	0.15	-0.28
DME molecule	0	0	0

A very different behavior is observed on the oxide and chloride surfaces. In these cases, no significant charge is transferred between the surface and the decomposed DME products, Table 3.2. The only charge transfer that occurs is between atoms in the DME fragments. The resistance to charge transfer from these ionic surfaces (i.e., oxidation) reflects their high stability. The outcome is that the DME fragments are not stabilized by charge transfer, and the decomposition reactions generate products whose energies are roughly equivalent to those of the unreacted DME molecule.

The reaction pathways for the gas-phase decomposition of DME were also examined. This was achieved by initializing a NEB calculation from the surface-mediated pathways shown in Figure 3.5, but with the surfaces removed from the computational cell (gas-phase decomposition based on the $MgCl_2$ pathway was not investigated, as it is expected to be similar to the analogous pathway on similarly-inert MgO). When initiated from the MgO pathway, these calculations reveal that the shape and reaction barrier for the gas-phase pathway are similar to those found on the surface. Earlier, it was mentioned that the reaction energy for DME decomposition on MgO is only slightly more exothermic than for the same reaction in the gas phase. The lack of charge transfer on MgO, in conjunction with the similarity of the reaction energies and energy barriers for the surface-mediated and gas-phase reactions, suggests that the MgO surface is essentially inert (i.e., does not aid significantly in the decomposition of DME). Conversely, the calculations aimed at evaluating the gas-phase DME decomposition pathway (as initialized from the Mg surface pathway) did not converge after ~4500 ionic relaxation steps. This behavior, combined with the large charge transfer and exothermic DME decomposition energy discussed previously, suggests that the Mg(0001) surface plays a significant role in mediating DME decomposition.

To summarize, DME decomposition is both thermodynamically and kinetically favorable on the pristine Mg surface. In contrast, the MgO and $MgCl_2$ surfaces are relatively inert. These results suggest that the performance of Mg anodes in DME-based electrolytes could be improved by evolving chloride- or oxide-based surface films, as these will hinder DME decomposition. Such a process would be analogous to the formation of an SEI on the anode of Li-ion batteries.[1] In Li-ion cells the formation of the SEI limits electrolyte decomposition, yet allows for the transport of Li-ions between the electrolyte and the underlying electrode. In Mg-ion systems, the possibility of forming a similarly functioning SEI has been debated.[1,8,78,112] For example, some surface films on Mg anodes have the potential to block the transport of Mg^{2+} across their thickness.[1,8,78] Nevertheless, recent work by Arthur *et al.*[112] suggests that the blocking behavior of Mg SEIs may

not be universal. In that study, magnesium deposition and stripping were examined in symmetrical Mg/Mg cells containing borohydride electrolytes. Evidence for the formation of an SEI was suggested by several surface characterization techniques. Notably, the formation of the SEI did not prevent magnesium deposition and stripping.

With regard to the surface compositions analyzed in this study, it is expected that Mg-ion diffusion through crystalline MgO would be slow.[113] Nevertheless, transport could be sufficiently fast if the oxide was very thin, amorphous, or porous.[114] We are aware of no measurements or calculations of Mg-ion diffusion through $MgCl_2$. However, since $MgCl_2$ is a layered material with large interplanar spacing along the ⟨0001⟩ direction, ion transport within these planes could potentially be fast. Earlier experimental work has shown that the formation of a Mg–Cl enhancement layer on the anode surface coincides with improved performance.[14,16] Undoubtedly, more detailed experimental characterization of the structure and composition of the "Mg SEI" will be helpful in clarifying the mechanisms responsible for efficient operation of Mg anodes.

3.4 Conclusions

Magnesium is a promising anode material for use in next-generation batteries because of its high energy density, abundance, and its reduced tendency to form dendrites. Nonetheless, the development of a practical Mg battery must overcome several challenges. Among these is the decomposition of the electrolyte solvent, which can contribute to passivation of the anode surface, thereby preventing reversible plating/stripping of Mg during battery cycling. This chapter has examined the thermodynamics and kinetics of electrode-mediated solvent decomposition in Mg batteries using first-principles calculations. The initial steps in the reaction pathway associated with decomposition of a model solvent, DME, on three relevant negative electrode surface compositions—Mg(0001), MgO(100), and $MgCl_2$(0001)—were examined.

These calculations have revealed two distinct scenarios for DME decomposition. On the metallic surface, solvent decomposition is highly exothermic and rapid, with ethylene gas predicted to evolve as a product. Reductive charge transfer from the Mg(0001) surface to the DME fragments aids in reducing kinetic barriers and stabilizes the decomposed state. On the other hand, both of the ionic MgO(100) and $MgCl_2$(0001) surfaces were observed to be relatively inert, with limited impact on solvent decomposition. Decomposition on these surfaces is approximately thermoneutral, indicative of a weak thermodynamic driving force for these reactions. The decomposition reaction pathways also exhibit large energy barriers, which are attributed to a slow

H-exchange process between fragments. Additional evidence for the limited role played by these surfaces can be found in the negligible amount of charge transferred between the surface and the adsorbed DME.

These outcomes have several important consequences for electrolyte/anode interfaces in Mg batteries:

1. Mg metal—whose presence can result from cracking/exfoliation of an existing SEI, or electro-deposition of Mg during charging—will readily decompose DME into ethylene gas and adsorbed methoxy fragments.
2. The resulting fragments may further evolve into adherent, stable phases (i.e., films comprised of oxides, hydroxides, carbonates, etc.) that are less likely to promote solvent decomposition.
3. Although the aforementioned films will slow the rate of solvent consumption, their ability to transport Mg ions during plating/stripping will determine whether they are helpful (as in an SEI) or harmful (i.e., passivating) to cell operation overall. These transport properties will be strongly influenced by the structure (crystallinity, porosity) and composition of the films. Unfortunately, these microstructural properties are difficult to predict at the level of first-principles calculations.
4. In the case of Cl-containing electrolytes, the present calculations support the hypothesis that a Mg–Cl enhancement layer on the anode surface can improve the performance by limiting solvent decomposition. Furthermore, the layered (vdW) structure of crystalline $MgCl_2$ may allow for facile Mg-ion transport. Thus, $MgCl_2$ may be an important component of a Mg anode SEI.

Ultimately, an ideal Mg anode should exhibit a surface film that limits solvent decomposition yet allows for the rapid transport of Mg^{2+} across its thickness. The development of strategies that balance these requirements will accelerate the commercialization of Mg-ion batteries.

Chapter 4: Adhesive strength of a graphene oxide membrane for lithium anode protection

4.1 Introduction

As discussed in the first chapter, Li metal is an attractive anode material, but its implementation in batteries is plagued by a number of challenges. Most notably, Li metal is susceptible to electrochemical reaction with the electrolyte and to dendrite formation. One potential solution to this challenge is to use a protective membrane on the anode surface. In recent years, a number of artificial SEI materials have been considered for use as a protection layer at Li metal anodes. These include: LiF,[18] Al_2O_3,[19–21] polymer coatings,[22–24] and carbon nanospheres.[25] The focus of many of these studies is on preventing dendrite formation at the anode in order to create safer batteries, and to improve the Coulombic efficiency by inhibiting reactions between the Li anode and the electrolyte.

It is common for the artificial SEI layer in these studies to be subsequently evaluated for its ability to transport Li ions, as this is one crucial factor for the successful implementation of an artificial SEI in a battery. Nonetheless, many of these materials are not well-suited for such an application. LiF and Al_2O_3 are poor ionic conductors.[26,27] Although very thin protective layers fabricated from these materials may still allow for the transport of Li^+, materials with improved ionic transport properties would provide improved performance. Further, all of the characteristics necessary for a protective membrane often are not considered collectively. In addition to exhibiting high Li-ion conductivity, such a membrane should have high mechanical strength to suppress dendrite nucleation, block the direct interaction of the anode with the electrolyte to prevent electrolyte decomposition, and exhibit little to no electronic conductivity.

Two-dimensional (2D) structures are a promising class of materials for a protective membrane. Owing to their thin, yet rigid structure, 2D materials possess high Li-ion transport properties and mechanical integrity.[28] Further, certain 2D materials may also block electrolyte decomposition and electron transport. One particular 2D material, graphene oxide (GO), has gained attention as a physically-blocking membrane that may exhibit all of these properties.[29–32] A GO membrane has

been shown to selectively transport ions, allowing Li^+ to pass through the membrane and blocking the transport of other species that can react with the anode, such as anions.[29] This is particularly relevant in Li-S batteries where polysulfides shuttled from the sulfur cathode may react with the Li anode to deplete the Li reservoir and decrease the Coulombic efficiency. In addition, GO allows a smoother layer of Li to form at the anode by "storing" dead lithium, effectively decreasing the tendency to form dendrites.[30] Furthermore, its thin structure does not significantly reduce the usable capacity of the battery. In a recent study employing a layered reduced graphene oxide, the anode retained ~3390 mAh/g of capacity (out of a total 3860 mAh/g mentioned above).[31]

Few modeling studies have analyzed the utility of employing a GO membrane for Li anode protection. Therefore, this chapter, which is one component of a larger study investigating GO for its suitability as a protective layer at Li metal anodes, analyzes one important property of the membrane – its work of adhesion with a Li metal surface. As will be shown, GO is strongly adhered to the Li metal surface in comparison to other phases or compounds present in the SEI. This result supports its use as a protective membrane.

4.2 Methodology

As in Chapter 3, DFT calculations were performed in VASP. The exchange−correlation energy was determined using three different functionals: the vdW-DF2 functional to account for dispersion interactions,[86–89] the functional of Perdew, Burke, and Ernzerhof (PBE),[46] and the PBE functional revised for solids (PBEsol).[115] Electronic wavefunctions were expanded in a plane wave basis, with a 440 eV energy cutoff, and the projector-augmented wave method was used to describe interactions between core and valence electrons.[51,52] The ions in each computational cell were allowed to relax until all forces were less than 0.04 eV/Å and the k-point mesh was set to 2 × 2 × 1. The simulation cells consisted of seven layers of Li atoms, two layers of GO, and a vacuum region. The structure of the GO layer is consistent with materials characterized experimentally.[116–118] Two oxidation states of GO were analyzed in this work, representing C:O ratios of 1.8 and 2.7. The Li(111) surface slab was chosen since it gave the lowest interfacial strain with GO among the low-index surfaces (100), (110), and (111). The simulation cells for both C:O ratios had dimensions of 8.43 Å × 9.73 Å.

The work of adhesion, W_{ad}, was computed using:[119–122]

$$W_{ad} = \sigma_{Li} + \sigma_{GO} - \gamma_{Li/GO} \tag{4.1}$$

where σ_{Li} and σ_{GO} are the surface energies of Li and GO in vacuum, and $\gamma_{Li/GO}$ is the energy of the interface formed when Li and GO are in contact with one another. This quantity was computed as the energy difference when the two slabs were roughly 10 Å apart ($\sigma_{Li} + \sigma_{GO}$) and when they were in contact with one another ($\gamma_{Li/GO}$). The work of adhesion could also be computed by calculating each of the terms in equation 4.1 separately. This method was also tested, and it was found that it modified the work of adhesion by only a small factor, 0.02 J/m^2.

The configuration used to calculate $\gamma_{Li/GO}$ was taken to be the one which minimized the energy due to translation in all three spatial directions. This was done by first calculating the gamma surface: specifically, the GO layer was translated in both directions parallel to the Li slab and the energy surface was traced out as a function of position. Then, using the lowest energy structure on the gamma surface as the starting configuration, we calculated a universal binding energy (UBER)[119–122] curve by incrementally modifying the distance between the two slabs in the direction perpendicular to the slabs. In this manner, the unrelaxed work of adhesion from the UBER curve was obtained by keeping all atoms in the simulation cell fixed. To compute the relaxed work of adhesion, all atoms were allowed to relax starting from the minimum configuration on the UBER curve and the van der Waals density functional, vdW-DF2, was employed to obtain relaxed configurations taking into account dispersion interactions. Finally, the dispersion-corrected configurations were used as input to recalculate W_{ad} with the other exchange−correlation functionals.

4.3 Results and discussion

As discussed in the Methodology Section, the lowest energy interfacial structure of the Li/GO system was determined by translating the slabs in all three spatial directions. Translation in the *x*- and *y*-directions resulted in a gamma surface, showing the energy of the system at a fixed distance in the *z*-direction. The gamma surface, as well as the portion of the slab for which the surface was generated, is shown in Figure 4a for the Li/GO interface with the lowest degree of oxidation (C:O=2.7). A similar result was obtained for the slab with a higher degree of oxidation. The lowest energy configuration corresponded to a translation of 0.05 Å in the *x*-direction and 0.3 Å in the *y*-direction.

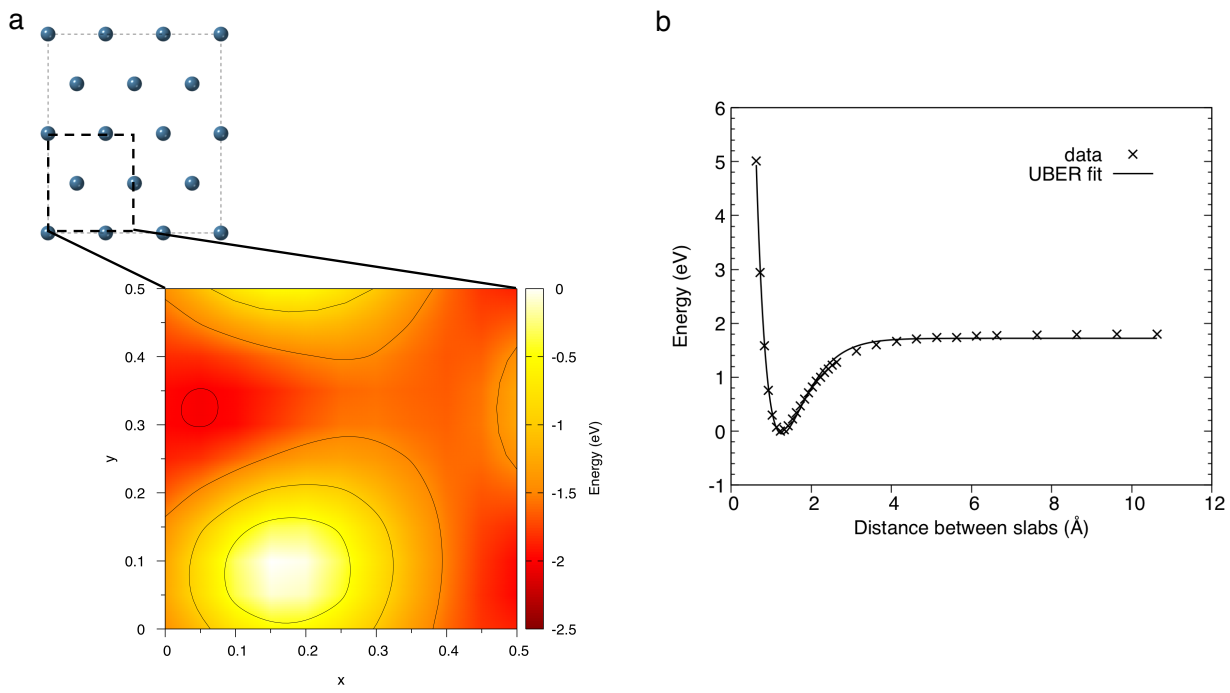

Figure 4.1 Determining the lowest energy configuration in all three spatial directions for the Li/GO interface having the lowest degree of oxidation (C:O=2.7). (a) Gamma surface of total energy vs. translation in the *x*- and *y*-directions (at a fixed distance in the *z*-direction between slabs). The portion of the slab traced out in the contour plot is shown with regard to the position of the Li atoms. (b) UBER curve for the same interface using the lowest energy configuration from the gamma surface as the starting configuration. Here, distance in the *z*-direction is varied while translation in the other two spatial directions is fixed.

Starting from the lowest energy structure on the gamma surface, the UBER curve for the configuration was created (Figure 4b). In this plot, the slabs were fixed from translating in the *x*- and *y*-directions but were moved in the direction perpendicular to one another (*z*-direction). The lowest energy structure on the UBER curve was reached when the two slabs were separated by a distance of 1.23 Å. As shown in Figure 4b, the UBER curve resulted in an accurate fit to the unrelaxed energies, showing that the interaction between slabs decreases at an exponential rate. When scaled by the area of the interface, the depth of the well on the UBER curve corresponds to the unrelaxed work of adhesion. In addition, the relaxed work of adhesion was obtained starting from the lowest energy structure on the UBER curve. The results for the work of adhesion computations are displayed in Figure 4.2 for the various functionals employed in the study.

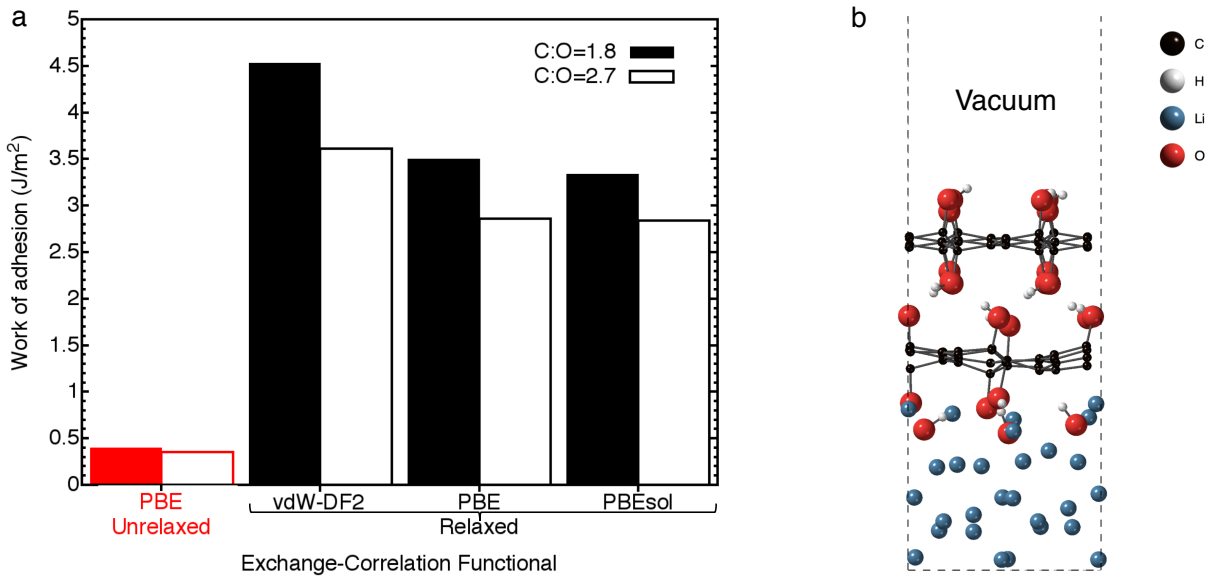

Figure 4.2 (a) Computed work of adhesion for the Li(111)/GO (C:O=1.8) and Li(111)/GO (C:O=2.7) interfaces. Results are shown for the unrelaxed (red) and relaxed (black) interfaces using various exchange−correlation functionals. (b) Relaxed interfacial structure for the Li(111)/GO (C:O=2.7) interface with the vdW-DF2 functional. There is significant mixing between Li and GO layers in the immediate vicinity of the interface.

As shown in Fig. 4.2, the work of adhesion is about 0.5-0.9 J/m^2 larger for the GO model that exhibits a larger degree of oxidation (C:O=1.8). From this result, there appears to be a strong interaction between O atoms in GO and the Li atoms in the Li slab. An examination of the relaxed interfacial structures at both C:O ratios confirms this assessment. Figure 4.2b shows that there is significant mixing from the atoms in the two slabs near their interface for C:O=2.7, and that the mixing appears to be due to hydrogen and oxygen atoms that are "drawn into" the Li layer. A similar result is obtained for C:O=1.8. This suggests that the strength of the binding at the interface can be tuned by modifying the oxygen content in the GO membrane.

To place the calculated adhesion behavior at the Li/GO interface in context, the relaxed energies were compared with those obtained for interfaces with other surface films explored in Li metal batteries – LiF and Li_2CO_3. LiF represents one coating strategy, whereas Li_2CO_3 is the outermost layer in the native oxide film on Li metal (see Figure 1.5 in Chapter 1). Based on our calculations in this study and in past work[123] using the same approach, the work of adhesion between Li metal and both of these materials is roughly an order of magnitude smaller than those obtained with GO. This finding was further confirmed by computations in the study of Liu *et al.*[6] The authors in that study also obtained work of adhesion energies for LiF and Li_2CO_3 interfaces with Li metal roughly an order of magnitude lower than those displayed in Figure 4.2a. This suggests that the Li/GO interface is strongly binding. Given how strong the binding is at the Li/GO

interface, we also computed the work of adhesion between GO layers. The results showed that it requires significantly less energy to separate a slab between GO layers (~0.42 J/m^2) than it does to separate a slab right at the Li/GO interface (>2.8 J/m^2).

As with the Li/GO interface, examining the relaxed interfacial structures for LiF and Li_2CO_3 with Li metal provides insight into the interfacial energetics. Specifically, there is no mixing of atoms between the two slabs in either interfacial model; only a slight distortion of the atoms at each interface is observed. This weak interaction leads to relatively low adhesion. From these results, it is possible to relate interfacial structure with interfacial energetics. In structures where O atoms (or other elements likely to strongly interact with Li) are loosely coordinated with a material, such as in the 2D GO structure, those O atoms are susceptible to being "drawn into" the Li layer and the interfacial adhesion is strong. On the other hand, when O atoms are more strongly coordinated with a surface, such as in Li_2CO_3, those O atoms interact weakly with the Li layer and the interfacial adhesion is correspondingly weak.

It is important to note that the GO model used for the work of adhesion calculations is ordered. Disordered GO models in which the epoxide and hydroxyl groups are randomly attached to the carbon backbone are also possible in nature. Although the work of adhesion of disordered configurations will likely vary from those computed for the ordered configurations discussed above, the trends are expected to be similar. For instance, regions of a disordered GO membrane where clusters of epoxide and hydroxyl groups exist may display stronger interfacial adhesion; similarly, regions where these surface groups are not present may display weaker interfacial adhesion than the values presented in Figure 4.2a.

Translating these findings to Li metal batteries, there is evidence to support the fact that strong wettability of a protective membrane by Li may reduce interfacial resistance.[123] The wettability of molten Li metal on a membrane can be related to the work of adhesion through the Young-Dupré equation: $W_{ad} = \sigma_{Li} (1 + \cos \theta)$. Here, σ_{Li} is the surface energy of Li and θ is the contact angle between molten Li and the GO surface. Using this equation, the contact angle Li makes with GO for each oxidation state is zero degrees. In other words, Li is predicted to fully wet the GO membrane, and interfacial resistance in a battery employing a GO protective coating is also predicted to be low. Thus, from the standpoint of adhesion, GO is a promising material for use in Li metal batteries.

4.4 Conclusions

Li metal is a highly attractive anode material in next-generation batteries owing to its high theoretical specific capacity, low density, and very negative redox potential. Yet, key challenges such as its propensity to react with the electrolyte and its tendency to form dendrites have limited its utility. A promising approach for solving these challenges is to employ an artificial membrane at the Li anode to suppress dendrite formation and block electrolyte reduction. This work provided an assessment of one of the properties of one such protection layer, a graphene oxide membrane. From our calculations, the GO membrane displayed a large work of adhesion at the Li/GO interface. In comparison to other common SEI materials, the GO membrane displayed a much larger adherence to the Li metal anode. It was shown that it is more likely for the structure to separate between GO layers than it is at the Li/GO interface.

The work presented in this chapter is one piece of a larger study assessing the properties of a graphene oxide membrane. Not included in this chapter is a rigorous analysis of the Li-ion conductivity, the elastic properties, and the electronic properties of the GO membrane. In order to provide a more thorough analysis of the suitability of a GO membrane as a protective layer at Li metal anodes, all of these properties should be considered collectively. Nonetheless, from the standpoint of adhesion, the GO membrane is a promising material.

Chapter 5: Modeling the interface between lithium metal and its native oxide

5.1 Introduction

In Chapter 1, lithium metal batteries (LMBs) were presented as one of the most attractive next-generation battery architectures due to their high specific capacities. In addition, LMBs have an extremely negative reduction potential at the anode, allowing for high voltage batteries, and Li ions display fast transport through solid electrodes. However, among the challenges for commercializing LMBs is the formation of an SEI layer that does not appear to be self-limiting (i.e., reaching a critical thickness at which electrolyte decomposition is prevented). Electrolyte decomposition occurs continuously in LMBs with traditional carbonate solvents, leading to a depletion of the electrolyte.[17,34,124–126] Even with solvents more suitable to use in LMBs, such as DOL:DME, electrolyte decomposition may occur. Electrolyte decomposition products, as evidenced by the components of the SEI, vary widely based on the composition of the electrolyte.[42]

In addition, Li-ion transport through the SEI can be a concern. In order for the battery to be successfully cycled, Li ions must be able to pass through the SEI. Nonetheless, many SEIs formed in LMBs have low ionic conductivity. Further, because Li^+ does not plate/strip evenly on the anode surface, dendrite formation occurs. An extensive body of work addresses the latter concern by applying various types of protection strategies on the Li metal anode to control the structure of the SEI. Some of these strategies are: two-dimensional membranes (Chapter 4), atomic layer deposition,[19–21] film-forming electrolyte additives,[33,127] electrode modification,[38] or using a solid electrolyte.[128] Due to all of these complications, the nature of the SEI layer in LMBs remains elusive. There is no universal SEI layer, and, even in SEIs formed in specific studies, the structure of the SEI is not well characterized.

To better characterize the SEI layer, we turn our attention to an underexplored feature: the native oxide layer on Li. Since Li metal is so reactive, it will have a native oxide layer present on its surface, even when fabricated in an oxygen-poor environment. Thus, the innermost SEI layer in a Li metal battery is the native oxide, Li_2O. This is the one component of the SEI which is

universal across all battery chemistries. Moreover, many studies attribute the cycling behavior of LMBs to components that are found in the native oxide layer on the Li metal surface.[33,34,36–39] In the Adams *et al*. study,[33] the authors showed that adding $LiNO_3$ to a state-of-the-art DOL:DME electrolyte in Li-S batteries led to an improvement in CE and cycle life. This improved behavior was attributed to the presence of Li_2O in the SEI on Li metal, which was suggested to inhibit the decomposition of salt and solvent species in the electrolyte. In recent work by Cui and co-workers, cryo-TEM was performed on a Li metal SEI in carbonate electrolytes with fluoroethylene carbonate (FEC)[34] and $LiNO_3$ additives.[36] In each scenario, the structure of the SEI was preferentially modified by the additives. With the additives, the SEI contained an inner, amorphous layer and an outer, ordered layer of Li_2O. This is in contrast to an SEI consisting of nanocrystalline regions in an amorphous matrix without the additives.

Based on the importance of the native oxide layer, previous computational studies have developed various models for the Li/Li_2O interface. Lepley and Holzwarth created two Li/Li_2O slab supercell models and computed the interfacial and strain energy in both systems.[129] Koch *et al*. carried out a simulated gas adsorption and surface incorporation algorithm on the three low-index Li surfaces with various atmospheric gases, including O_2.[130] The authors analyzed the structural, electronic, and elastic properties of the various interfaces. Nonetheless, a rigorous characterization of the structure of the Li/Li_2O interface and its effect on Li-ion transport is missing.

In the current chapter, realistic models for the interface between Li metal and its native oxide are constructed. First, low strain slab supercell models are constructed based on low energy surface terminations. Second, a simulated oxidation algorithm is employed for incorporating O_2 molecules into a Li slab (oxidized slab model). The structures of the slab supercell and oxidized slab models are characterized using radial distribution functions, charge transfer analysis, and shifts in Li core-level electron binding energies. As oxidation progresses in the oxidized slab model, the structure of the interface approaches that of the slab supercell model. Nevertheless, the oxidized slab model retains an amorphous structure.

Next the Li^+ transport properties of the interface models are assessed with AIMD simulations at a range of temperatures. The Li^+ diffusivities indicate fast transport of Li ions across the interface when compared with other compounds commonly found in LMB SEIs. The interface models presented in this paper represent an accurate reconstruction of the Li metal/native oxide layer. At the native oxide layer thicknesses considered in this study (~ 2 monolayers), the native oxide layer

supports the fast transport of Li ions. Combined with a rigorous analysis of the mechanical and chemical properties of this interface, the native oxide layer may constitute a beneficial component of the SEI.

5.2 Methodology

All calculations, as in previous chapters, were performed using density functional theory, as implemented in VASP. The exchange−correlation energy was accounted for using the PBE functional, the projector-augmented wave method was used to describe interactions between core and valence electrons, a 440 eV plane wave energy cutoff was used, and the force minimization criterion was set at 0.04 eV/Å. The k-point mesh was set to 2 × 2 × 1 for total energy calculations and 6 × 6 × 1 for core-level binding energy shift calculations.

5.2.1 Slab supercell model

The Li/Li_2O slab supercell model was constructed by starting with the lowest energy Li_2O surface, Li_2O(111), as determined in a previous study.[131] The Li(111) surface slab was chosen since it gave the lowest interfacial strain with Li_2O(111) among the low-index surfaces (100), (110), and (111). For the Li_2O slab, both a Li-terminated, stoichiometric slab and an O-terminated, oxygen-rich slab were created. In both cases, the Li/Li_2O interface was constructed by straining a 3 × 3 Li_2O(111) supercell by 1.12% to match a 2 × 2 Li(111) supercell. The interface cell consisted of two equivalent interfaces with dimensions of 9.73 Å × 9.73 Å.

The relaxed structure of the interface cell was determined by initially minimizing the energy due to translation in all three spatial directions. As in Chapter 4, this involved a gamma surface calculation followed by a calculation of the UBER curve. Then the entire interface cell was relaxed by allowing both the atom positions and the lattice parameters to change. This fully relaxed structure was used for computing the formation energy. For the interface involving a stoichiometric Li_2O slab, the formation energy is:

$$E_F = \frac{E_{Li/Li2O} - n_{Li}^{Li(BCC)} \mu_{Li}^{Li(BCC)} - n_{Li2O} E_{Li2O}}{2A} \quad (5.1)$$

where $E_{Li/Li2O}$ is the energy of the fully relaxed, two interface cell, $n_{Li}^{Li(BCC)}$ is the number of Li atoms in the Li slab, $\mu_{Li}^{Li(BCC)}$ is the chemical potential of Li in bulk Li metal, n_{Li2O} is the number

of formula units of Li_2O in the Li_2O slab, E_{Li2O} is the bulk energy of one formula unit of Li_2O, and $2A$ is the combined area of both interfaces. The interfacial energy was then determined using a method originally described by Wolverton and co-workers to separate the strain energy from the interfacial energy.[132] Based on this method, the interfacial energy for the stoichiometric system was computed as:

$$\sigma = \frac{E_{Li/Li2O} - n_{Li}^{Li(BCC)}\mu_{Li}^{Li(BCC)} - n_{Li2O}E_{Li2O(\mathbf{c})}}{2A} \tag{5.2}$$

where $E_{Li2O(c)}$ is the energy of a formula unit of bulk Li_2O in which the **a** and **b** lattice vectors have been strained to match their values in the interface cell so that only the **c** lattice vector is relaxed. In this equation, both the energy of the interface cell and the energies of the bulk system references include the same strain energy, so that the strain contribution is effectively removed from the system. Note that the Li_2O slab was strained to match the lattice parameters of the Li slab when forming the interface. Therefore, the Li slab does not include a strain energy. The strain energy (per atom) can then be calculated from the formation and interfacial energies:

$$\zeta = \frac{2AE_F}{N} - \frac{2A\sigma}{N} \tag{5.3}$$

where N is the number of atoms in the cell. For the interface involving an oxygen-rich Li_2O slab, there is not a formula unit-equivalent number of Li and O atoms in the Li_2O slab, and the equation for the formation energy involves more terms:

$$E_F = \frac{E_{Li/Li2O} - n_{Li}^{Li(BCC)}\mu_{Li}^{Li(BCC)} - n_{Li}^{Li2O}\mu_{Li}^{Li2O} - n_O\mu_O^{Li2O}}{2A} \tag{5.4}$$

where n_{Li}^{Li2O} is the number of Li atoms in the Li_2O slab, μ_{Li}^{Li2O} is the chemical potential of Li in bulk Li_2O, n_O is the number of oxygen atoms in the Li_2O slab, and μ_O^{Li2O} is the chemical potential of oxygen in bulk Li_2O. In equation 5.4, there are two unknown terms, μ_{Li}^{Li2O} and μ_O^{Li2O}. However, these two terms must add up (when weighted by their stoichiometric amounts) to the energy of a formula unit of bulk Li_2O as:

(5.5) $$E_{Li2O} = \mu_O^{Li2O} + 2\mu_{Li}^{Li2O}$$

Thus, there is only one independent variable. We computed the formation energy by specifying this variable at two extremes, representing two equilibrium conditions. Under equilibrium condition one, the chemical potential of Li in Li_2O (μ_{Li}^{Li2O}) is set at its value in bulk Li ($\mu_{Li}^{Li(BCC)}$). For equilibrium condition two, the chemical potential of O in Li_2O (μ_O^{Li2O}) is set at its value in oxygen gas ($\mu_O^{O2(g)}$). Plugging equation 5.5 into the last two terms in the numerator in equation 5.4 for both equilibrium conditions gives:

Equilibrium condition 1: $\mu_{Li}^{Li2O} = \mu_{Li}^{Li(BCC)}$

(5.6) $$E_F = \frac{E_{Li/Li2O} - n_{Li}^{Li(BCC)}\mu_{Li}^{Li(BCC)} - n_{Li}^{Li2O}\mu_{Li}^{Li(BCC)} - n_O\left(E_{Li2O} - 2\mu_{Li}^{Li(BCC)}\right)}{2A}$$

Equilibrium condition 2: $\mu_O^{Li2O} = \mu_O^{O2(g)}$

(5.7) $$E_F = \frac{E_{Li/Li2O} - n_{Li}^{Li(BCC)}\mu_{Li}^{Li(BCC)} - n_{Li}^{Li2O}\left(1/2E_{Li2O} - 1/2\mu_O^{O2(g)}\right) - n_O\,\mu_O^{O2(g)}}{2A}$$

The interfacial energy was also determined for the oxygen-rich systems using Wolverton's method.

5.2.2 Oxidized slab model

The oxidized slab model was created by starting with the same 2 × 2 Li(111) supercell as in the slab supercell model. Then, using a procedure informed by a study conducted by the Finnis group on a TiN(100) surface,[133] O_2 molecules were sequentially added (at rest) 3.0 Å above the Li(111) surface at the same position in the simulation cell. The system was dynamically evolved with a 4 ps AIMD simulation in the canonical (NVT) ensemble at 300 K following each O_2 molecule addition. The bottom 3 Li layers were fixed at their bulk positions. A time step of 1 ps was used and a Nosé thermostat[134] was employed with a mass of ~50 amu·Å^2, or an SMASS = 0.30. In total, 11 O_2 molecules were added, amounting to a surface coverage of greater than 2

monolayers. Between the addition of 6 and 7 O_2 molecules, 5 additional Li layers were added to the bottom half of the Li slab in order to allow for more O_2 molecules to be added to the top half of the simulation cell.

Once the oxidized slab model was generated, several analyses were performed on it. Charge transfer between the Li surface and the incorporated O atoms was analyzed using the Voronoi charge partitioning scheme. In comparison to the Bader charge partitioning implemented in Chapter 3, which partitions charges based on minima in the charge density profile, Voronoi partitioning assigns charges based on geometrical considerations. In this method, charge is partitioned by Voronoi polyhedra. This choice was made since the Bader analysis partitioned charge to atoms nearly 2 Å away, resulting in unphysical charges on Li atoms. Voronoi charge analysis was performed following the incorporation of each O_2 molecule into the Li surface (and the subsequent 4 ps AIMD simulation). In addition, Voronoi charge analysis was also performed on the relaxed, stoichiometric slab supercell system.

Computational shifts in Li 1s core-level electron binding energies were also calculated for each geometry following the incorporation of an O_2 molecule and in the stoichiometric slab supercell system. This analysis, which can be related to the binding energy of an electron obtained from XPS, enables one to distinguish between different structural and electronic environments experienced by a Li atom (i.e., Li 1s electrons in Li metal versus Li 1s electrons in Li_2O). The core-level binding energy shifts were computed using the final state and transition state methods.[55] In the former case, one full electron is excited from the core to the valence or conduction band; the energy difference between the core-excited state and the ground state is used to obtain the binding energy. In the transition state method, one-half of an electron is excited to the valence or conduction band and the eigenvalue of the core state for which the half electron was excited is used to obtain the binding energy.

Also, following the incorporation of the final O_2 molecule, an additional 10 ps AIMD simulation at 300 K was performed on the configuration. This was followed by a 4 ps annealing run at 600 K and a 4 ps cooling run again at 300 K. All other parameters in these simulations are consistent with those mentioned above. The final configuration from this round of simulations was then used for computing Li-ion diffusivities. For this analysis, AIMD was conducted at five different temperatures (600, 800, 900, 1100, and 1200 K) for a total of 40 ps at a time step of no greater than 3 fs. Results were then used to compute the MSD of all non-fixed Li atoms in the oxidized slab, which enabled computation of the diffusion coefficient at each temperature.

5.3 Results and discussion

5.3.1 Constructing the slab supercell model

As discussed in the Methodology section, two models for the Li/Li_2O interface were considered: one with a stoichiometric Li_2O surface and the other with an oxygen-rich Li_2O surface. A plot of the formation and interfacial energies for both models is given in Figure 5.1. The x-axis in Figure 5.1, $\Delta\mu_O$, is the change in the chemical potential of oxygen with respect to its energy in oxygen gas, O_2. The lower and upper bounds represent equilibrium conditions 1 and 2, respectively. The total, theoretical change in oxygen chemical potential is governed by the formation energy of bulk Li_2O, which was computed from DFT to be -6.00 eV. Therefore, if all energy is lowered in O when forming Li_2O, $\Delta\mu_O$ = -6.00 eV, the chemical potential of Li in Li_2O would be fixed at its value in Li metal and there is an equilibrium between Li atoms (lower bound). On the other hand, if all of the energy is lowered in Li when forming Li_2O, there is an equilibrium between O atoms in O_2 and in Li_2O (upper bound).

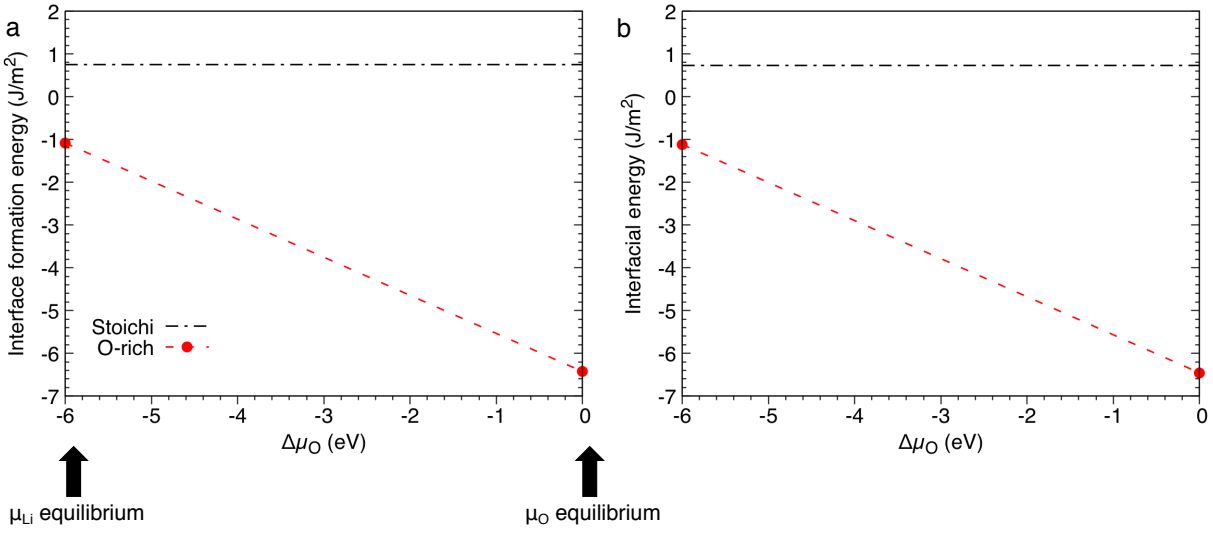

Figure 5.1 (a) Formation and (b) interfacial energies for Li/Li_2O slab supercell models with oxygen-rich (red dashed line) and stoichiometric (black dash-dotted line) Li_2O surfaces. The x-axis is the change in oxygen chemical potential with respect to its value in O_2 (g). The x-axis range (-6.00 eV) is set by the DFT-computed formation energy of bulk Li_2O; its lower bound represents equilibrium condition 1 and its upper bound represents equilibrium condition 2.

From Figure 5.1, the oxygen-rich system is always lower in energy than the stoichiometric system. This is likely attributed to a strong interaction between the O-terminated, oxygen-rich Li_2O surface slab and the Li metal slab. Additionally, the difference in formation and interfacial energies is so small that it cannot be seen at this scale. As the difference between these two energies is given

by the strain energy (0.017 J/atom in the stoichiometric system), this confirms the fact that this interface has very low strain.

5.3.2 Constructing the oxidized slab model

Each O_2 molecule incorporated into the Li slab when constructing the oxidized slab model eventually dissociated on the surface, but the time for this dissociation to occur varied as the oxidation progressed. Figure 5.2a,b shows the amount of simulation time required for each molecule to dissociate during O_2 incorporation. Also, Figure 5.2c displays the adsorption energy for each O_2 molecule. The adsorption energy was calculated as an energy difference between the current geometry and the previous geometry (with one less O_2 molecule incorporated) plus an isolated O_2 molecule. Each configuration was relaxed (at zero Kelvin) before performing the adsorption energy calculation.

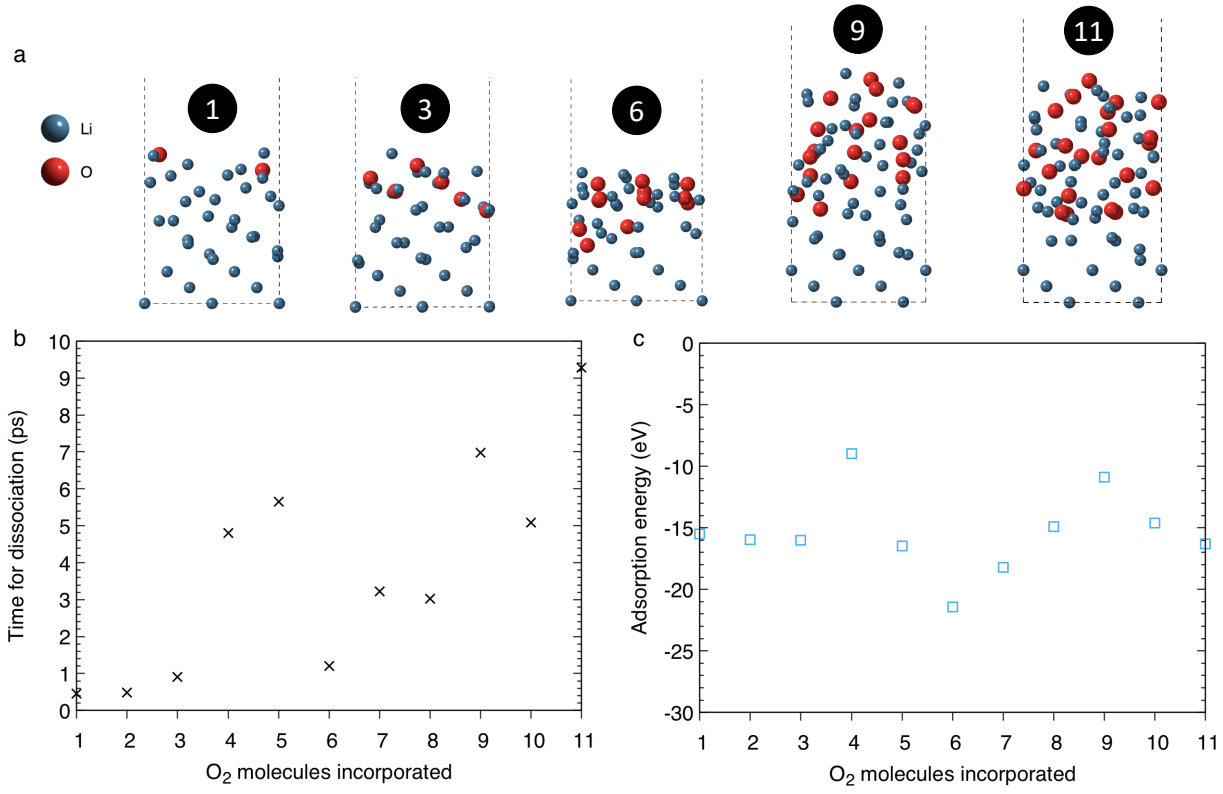

Figure 5.2 (a) Snapshots displaying the progression of O_2 incorporation into the Li slab, (b) simulation time required before each O_2 molecule is dissociated on the Li surface, and (c) adsorption energy progression with O_2 incorporation. Note: the slab is enlarged to include 5 additional Li layers between the incorporation of 6 and 7 O_2 molecules. Li and O atoms are colored blue and red, respectively.

Starting with Figure 5.2a, O atoms do not appear to be hindered from diffusing deep into the slab as oxidation proceeds. Furthermore, there is a contraction of the oxidized slab in moving from 1 to 6 O_2 molecules incorporated. This behavior is predicted to occur since Li_2O is denser than Li. In Figure 5.2b, dissociation time approximately increases with increasing oxidation. With increased oxidation, less Li atoms are available at the surface to facilitate in dissociation of an O_2 molecule. Additionally, with increased oxidation, O diffusion proceeds by newly incorporated O_2 molecules pushing existing oxygen atoms deeper into the slab. Lastly, Figure 5.2c shows that adsorption energy is roughly constant during the oxidation progression, oscillating around a value of about -15 eV/molecule.

5.3.3 Structural analysis

With all of the Li/Li_2O interface models constructed, the structures in each of these models were analyzed and compared. Starting with a qualitative analysis of the final relaxed structures (Figure 5.3), the oxidized slab model displays a more amorphous appearance than the other two structures. Although this result is mostly obvious since the two slab supercell models were initially constructed by interfacing crystalline materials, it is meaningful to more quantitatively assess the structural differences in the various models.

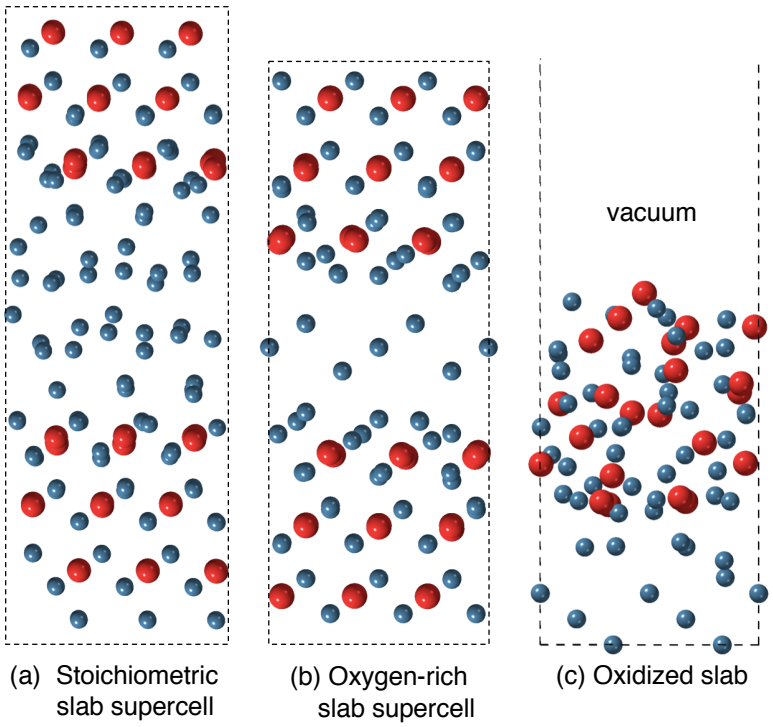

Figure 5.3 Relaxed structure of the (a) stoichiometric slab supercell model, (b) oxygen-rich slab supercell model, and (c) oxidized slab model (11 O_2 atoms incorporated). The coloring scheme is the same as in Figure 5.2.

A number of quantitative analyses were performed on the oxidized slab model, starting with the radial distribution function (RDF). The RDF was computed over the last 1,000 time steps in the AIMD simulation (amounting to 1 ps) in the oxidized slab. For comparison, a 1 ps AIMD simulation (1,000 time steps total) was also performed on crystalline Li_2O at 300 K, which was subsequently used for computing the RDF. Results are shown in Figure 5.4.

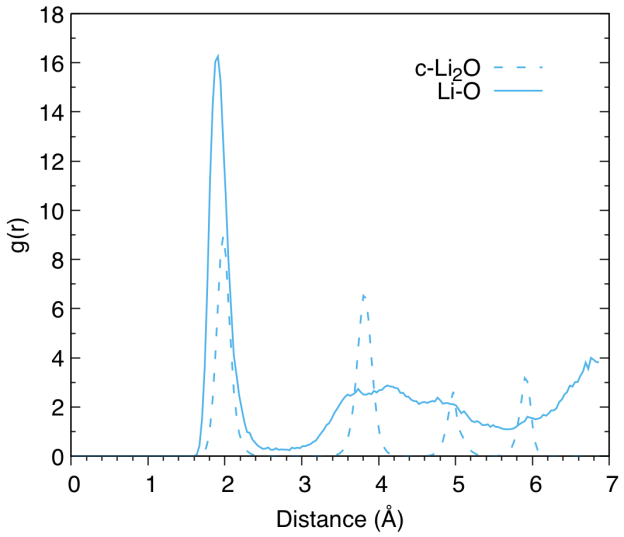

Figure 5.4 Radial distribution function for Li-O interaction in the oxidized slab model (solid line) and in crystalline Li_2O (dashed line).

The nearest neighbor Li-O bond distances in the oxidized slab roughly align with those in crystalline Li_2O. However, beyond the nearest neighbor distance, there is not much alignment between the two structures. This suggests that there is short range order, but not long range order in the oxidized slab model, which is characteristic of amorphous materials. This analysis was also conducted for the O-O interaction and a similar trend was observed. Next, we analyzed charge transfer between the Li slab and the O atoms in the oxidized slab and stoichiometric slab supercell models. The stoichiometric model was chosen for comparison since both slab supercell models have similar structure, but the stoichiometric model has a larger Li layer, making it easier to distinguish between Li metal and Li_2O regions. The Voronoi charges as a function of oxidation progression in the oxidized slab and stoichiometric slab supercell models are displayed in Figures 5.5 and 5.6, respectively.

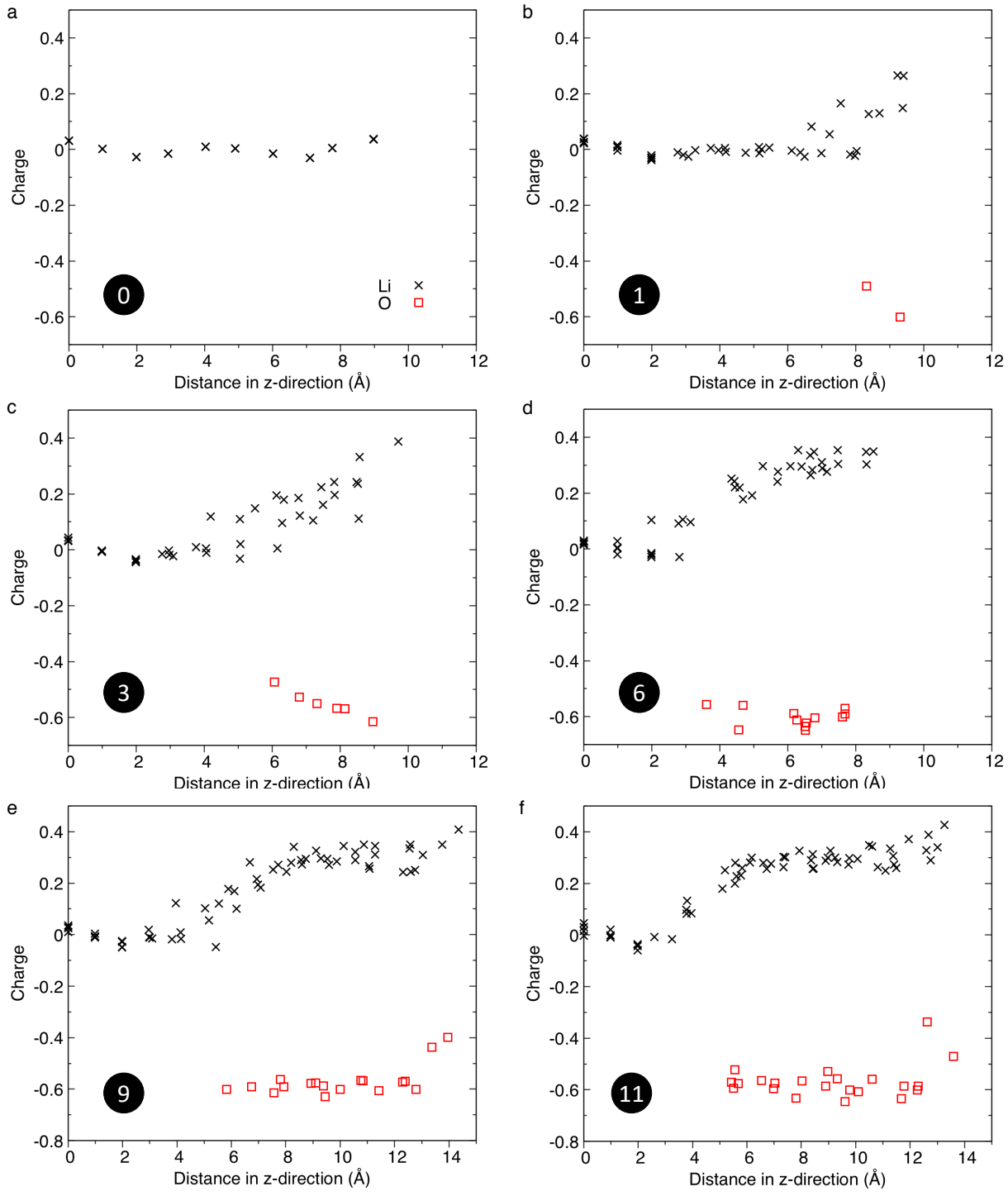

Figure 5.5 Voronoi charges in the oxidized slab model for (a) 0, (b) 1, (c) 3, (d) 6, (e) 9, and (f) 11 O_2 molecules incorporated. The charges on Li and O atoms are displayed as black Xs and red squares, respectively.

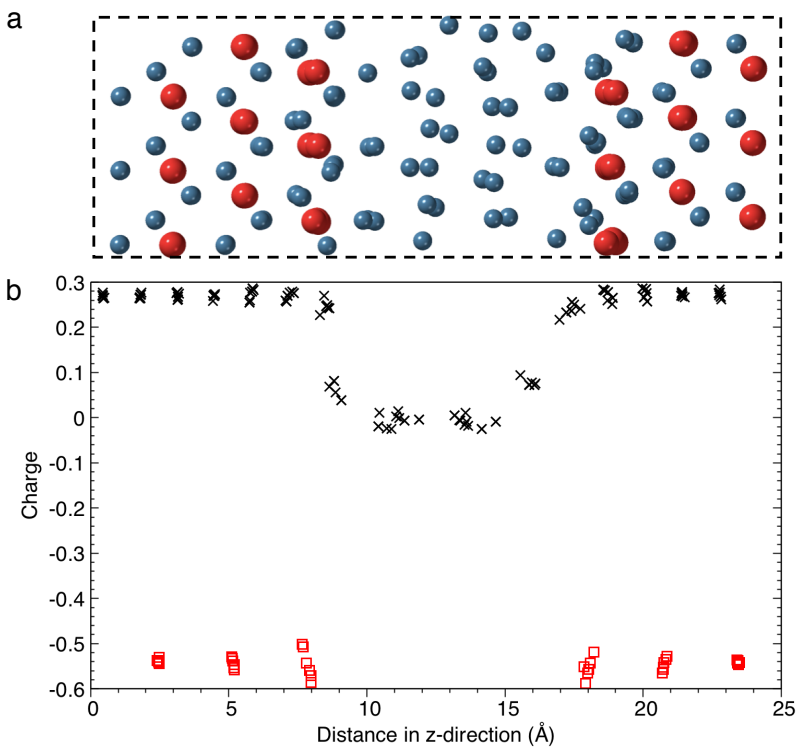

Figure 5.6 (a) Stoichiometric slab supercell model and (b) corresponding Voronoi charges. Li and O atoms are displayed in the same format as in Figure 5.5.

Turning first to Figure 5.5a, the charges on the Li slab before any O_2 molecules are added to the system are roughly zero, in line with what would be expected for a metallic system. As oxidation progresses, Li atoms in the portion of the slab exposed to oxidation (right side of the plots in Figure 5.5) transfer charge to the incorporated O atoms. A clear transition in the charge state of Li atoms is observed at the point in the slab to which O atoms have penetrated. Li atoms that have transferred some electron density to O atoms take on a charge of roughly +0.30. Similarly, each O atom pulls roughly a constant charge from the surrounding Li atoms, equivalent to a charge of around -0.60, exactly balancing the charge given up by the Li atoms. Of note, in each of the more oxidized configurations (9 and 11 O_2 molecules), two O atoms right at the surface (likely the most recently incorporated O_2 molecule) have pulled only about 0.40 electrons each from the surrounding Li atoms. This finding is in line with the increased time for O_2 dissociation as oxidation progresses (Figure 5.2b). As the slab becomes more heavily oxidized, the most recently incorporated O_2 molecules must diffuse to greater distances in order to pull electron density from Li atoms and dissociate.

In addition, similar to the observations made from a visual analysis of the configurations in Figure 5.2a, O atoms do not remain on the surface but are able to diffuse deeper into the slab as

oxidation progresses. Also, a contraction in the slab size is observed in going from 1 to 6 O_2 molecules incorporated. The total size decreases from around 9.5 Å to around 8 Å. Further, in moving from 9 to 11 O_2 molecules, the total size of the slab remains relatively constant, suggesting that the slab is densifying as it becomes more heavily oxidized. As previously mentioned, this is expected in transitioning from Li metal to an oxidized structure.

Looking at Figure 5.6, in the Li_2O portion of the interface, just under 0.30 e^- are transferred from each Li atom to the O atoms, resulting in a charge on each O atom of just under -0.60. In the Li metal portion of the interface, the system is roughly charge neutral. The amount of charge transferred in this crystalline model matches the charge transferred in the oxidized slab model in Figure 5.5. Consequently, the amorphous, oxidized slab model behaves much like the crystalline model from the standpoint of charge transfer. Nevertheless, one difference between the two models is that the transition region from Li metal to oxide is more abrupt in the crystalline model.

Shifting attention to the next analysis, the DFT-computed shift in core-level 1s electron binding energies is shown in Figures 5.7 and 5.8 for oxidized slab configurations and the stoichiometric slab supercell model, respectively. Since binding energy shifts give greater accuracy than absolute binding energies, the shifts relative to the binding energy in bulk Li metal are displayed.

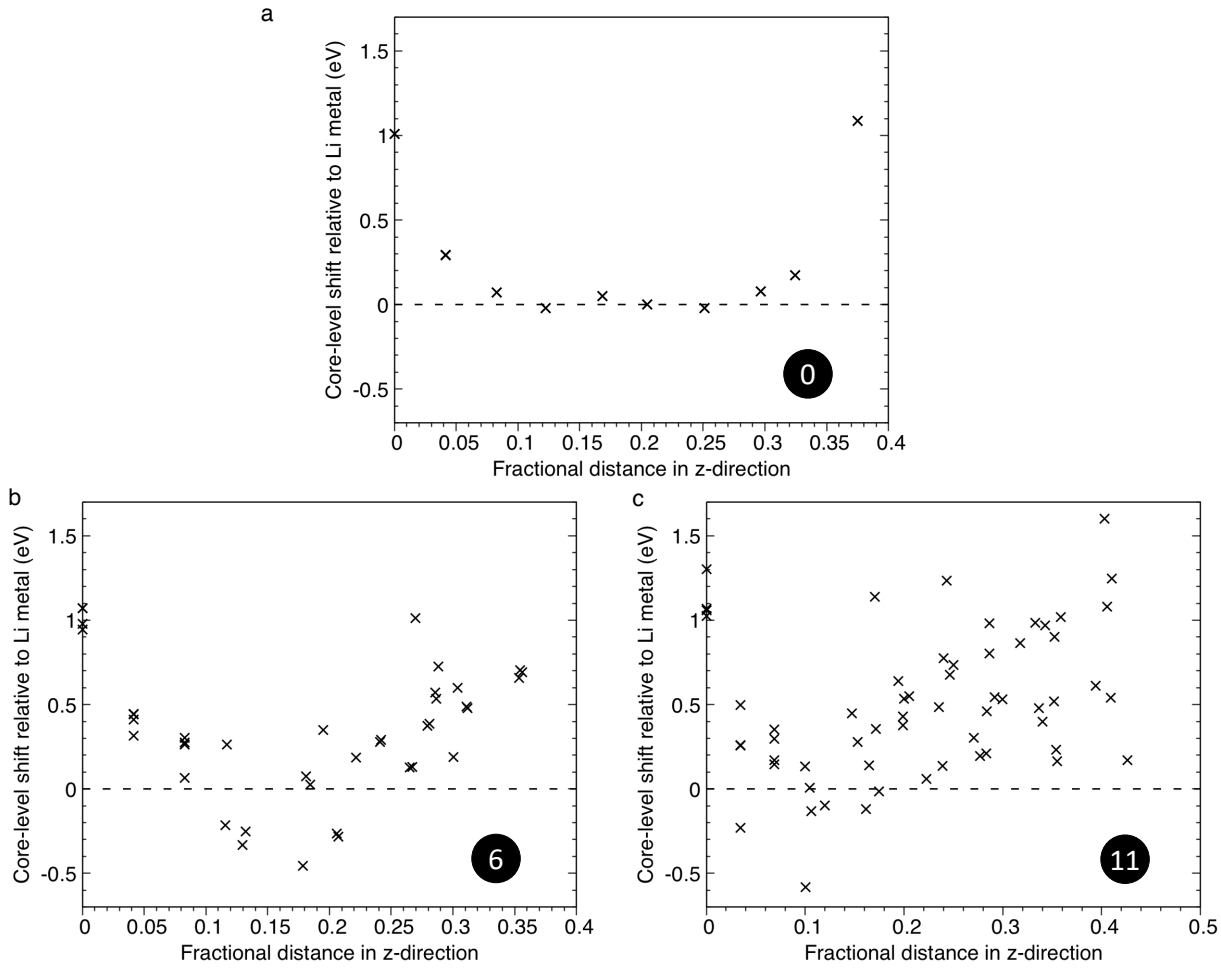

Figure 5.7 Computed shift in core-level electron binding energies for Li 1s electrons using the final state approximation in the oxidized slab model for (a) 0, (b) 6, and (c) 11 O_2 molecules incorporated. Binding energies are displayed with respect to the Li 1s level in bulk Li metal.

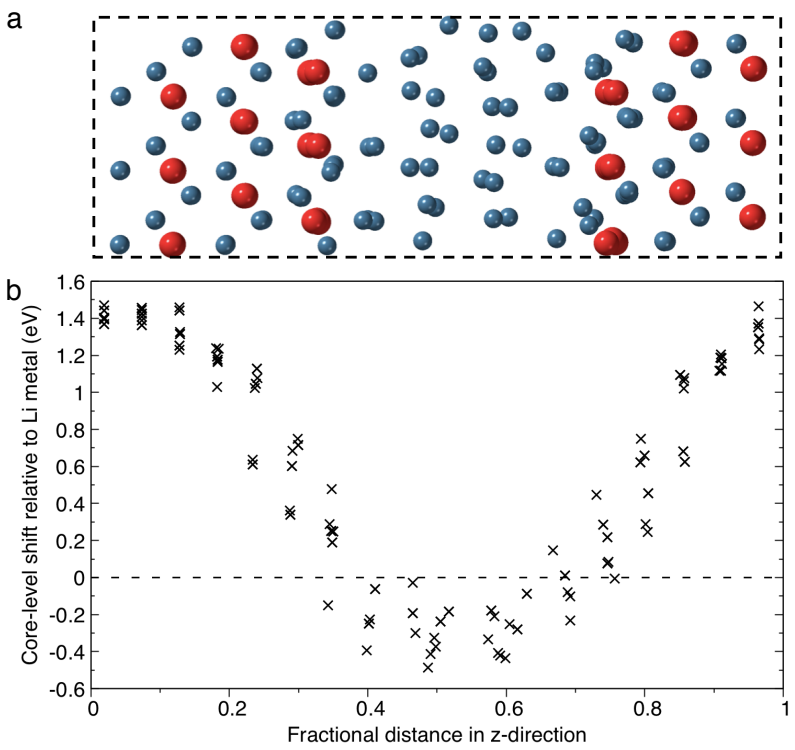

Figure 5.8 (a) Stoichiometric slab supercell model and (b) corresponding computed shifts in core-level electron binding energies for Li 1s electrons using the transition state method. As in Figure 5.7, binding energies are displayed with respect to the Li 1s level in bulk Li metal.

In the oxidized slab model with 0 O_2 molecules incorporated (Figure 5.7a), the electron binding energies in the bulk region of the cell show very good agreement with the computed electron binding energy in bulk Li metal. During O_2 incorporation (Figure 5.7b,c), the binding energies shift upwards in the portion of the slab exposed to the O_2 molecules. This is expected since the Li 1s electrons are more tightly bound in Li_2O than in Li metal due to reduced electrostatic repulsion from the 2s electrons that have been transferred to oxygen. There is also an observable shift downwards in the bulk Li metal portion of the slab during O_2 incorporation as the Li atoms move away from their equilibrium positions in Li metal. The overall range in binding energies in the most heavily oxidized model is around 1.5 eV. Experimentally, the core electron binding energy in Li_2O is about 2 eV higher than in Li metal (see Figure 2.1). Considering the experimental standard deviation in these values (> 1 eV in Li metal and Li_2O), there is reasonable agreement between computation and experiment.

Binding energies in the stoichiometric slab supercell model (Figure 5.8) show a very similar trend. The Li_2O portion of the interface exhibits binding energies about 1.7 eV higher in energy than those in the Li metal region, also in good agreement with experiment. As with the charge

distribution, the amorphous and crystalline models portray very similar results, with the main difference between the two being a more abrupt transition region from Li metal to oxide. Taken together, the charge state and electron binding energies are able to quantitatively distinguish between Li atoms in the metallic region of the interface and those in the oxide region. These analyses allow one to track the progression of oxidation in a Li film, as was demonstrated in Figures 5.5 and 5.7.

As a final structural analysis, the work of adhesion for the two slab supercell models, stoichiometric and oxygen-rich, was calculated following the procedure specified in Chapter 4. Results are shown in Figure 5.9. The stoichiometric interface exhibits moderate adhesion; energies are an order of magnitude lower than those of the GO interfaces in Chapter 4, but larger than those of the LiF and Li_2CO_3 interfaces in the study of Liu *et al*.[6] On the other hand, the oxygen-rich interface is the most strongly adhered of all of the interfaces analyzed in this dissertation, with a relaxed value more than three times greater than that of the most strongly adhered GO interface using the same exchange−correlation functional. The reason for this appears to be two-fold. First, as discussed when computing the interfacial energy, the O-terminated surface interacts very strongly with the Li metal surface. Second, the O-terminated Li_2O surface is very high in energy.

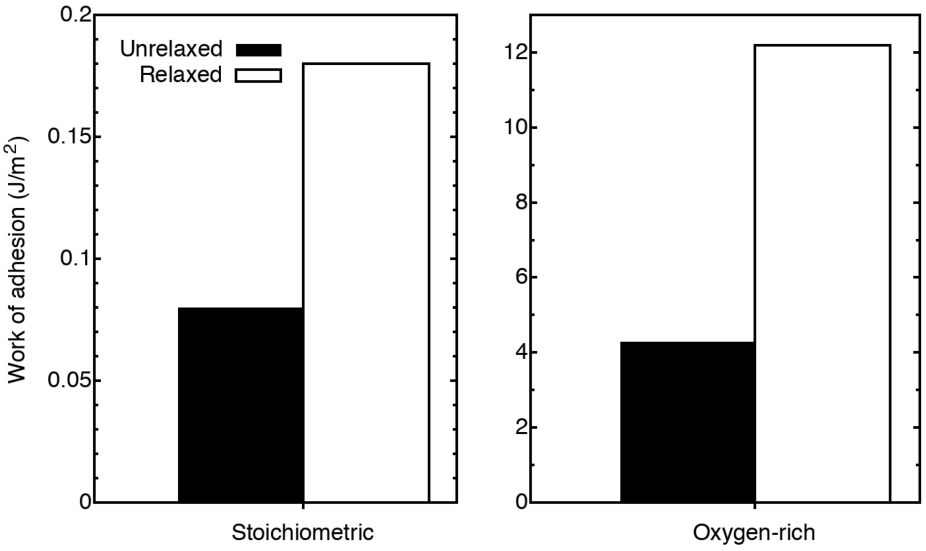

Figure 5.9 Computed work of adhesion energies for the stoichiometric and oxygen rich Li(111)/Li_2O(111) interfaces using the PBE functional.

5.3.4 Li-ion transport

After developing models for the native oxide layer, we then turned our attention to properties of the native oxide layer that are relevant in batteries. One property which has come up throughout this dissertation is ionic transport. For LMBs, it is crucial that Li ions are able to be transported to and from the anode during plating and stripping. Thus, we computed the diffusivities of Li in the oxidized slab model using AIMD at a range of temperatures. In order to sample the diffusional displacement regime of Li, we performed AIMD at high temperatures. Figure 5.10 shows the MSD of Li atoms and an Arrhenius plot of the computed diffusivities. Only the diffusional displacement regime was used to determine the diffusivities, which roughly corresponds to Δt = 10-20 ps. This regime represents the long time diffusion of Li, as opposed to the local vibrational motion in short time scales.

Considering that the nearest neighbor distance between Li atoms in crystalline Li_2O is around 2.3 Å, the squared displacement for a Li atom to move from its lattice position to the nearest site is roughly 6.76 $Å^2$. This value corresponds to the minimum MSD in order to sample diffusional displacement. In Figure 5.10a, all temperatures reach this value with the exception of 600 K. This justifies the use of higher temperatures. From the slope of the fitted line in Figure 5.10b, the activation energy for diffusion, E_a, is calculated to be 0.19 eV. This low activation barrier suggests fast Li-ion transport in the oxidized slab.

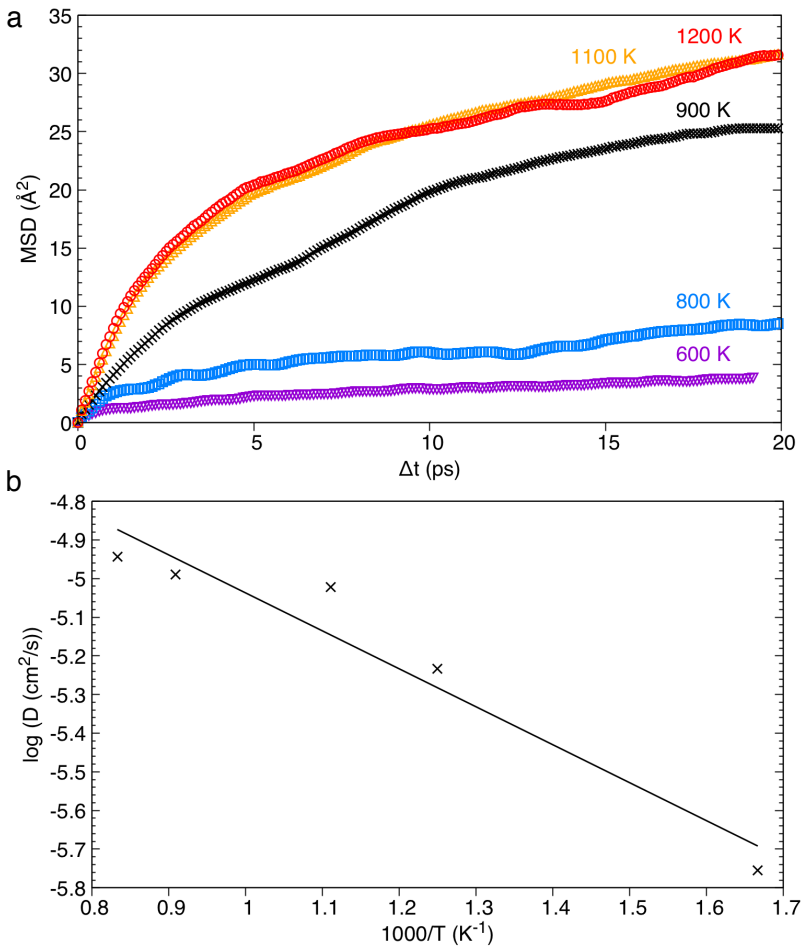

Figure 5.10 (a) Mean-squared displacement of non-fixed Li atoms in oxidized slab model with 11 O_2 molecules incorporated at 600, 800, 900, 1100, and 1200 K. (b) Arrhenius plot of Li-ion diffusivities at each temperature as determined from the diffusional displacement regime.

5.4 Conclusions

As highlighted in Chapter 4, Li metal anodes have received a great deal of attention for next-generation battery chemistries. A key challenge preventing the implementation of Li metal anodes is the structure of the SEI. The SEI should prevent electrochemical reaction with the electrolyte, possess high Li^+ transport, and suppress dendrite formation for successful battery operation. Although the composition of the SEI varies across electrolytes, one component that is expected to constitute the innermost SEI layer in virtually any battery employing a Li metal anode is the native oxide layer, Li_2O. Many experimental studies have attributed important cycling behavior of LMBs to the native oxide layer present on the Li metal surface. However, studies that assess the native oxide layer are rare. The current study provides one of the first detailed analyses of the native oxide layer.

In this chapter, the native oxide layer was modeled with a crystalline slab supercell interface and with an amorphous interface. The latter interface was generated by employing a simulated oxidation algorithm on a Li metal surface. The structures of the models were quantitatively characterized using radial distribution functions, Voronoi charge analysis, computed core electron binding energy shifts, and the work of adhesion. These analyses were able to distinguish between Li atoms in a metallic environment versus atoms in an oxide environment. In the oxidized slab model, this allowed us to track the progression of oxidation as O_2 molecules were incorporated into the surface. As the oxidized slab became more heavily oxidized, the structure of the interface approached that of the stoichiometric slab supercell model. Yet, the transition from metal to oxide was more abrupt in the slab supercell model as compared to the amorphous, oxidized slab structure.

An analysis of Li^+ diffusion in these models showed that the native oxide layer supports the fast transport of Li^+. Therefore, in line with some recent experimental observations, the native oxide layer may be a beneficial component in the SEI. Further work is needed to characterize other aspects of the native oxide layer, such as the mechanical and chemical properties, before the overall impact of the native oxide layer can be fully understood.

Chapter 6: Conclusions and future work

Renewable energy production is receiving increased emphasis in the 21st Century. In line with this thrust, there is an increasing demand for energy storage technologies with ever greater storage capacities. Batteries have emerged as one important technology, but the performance of the state-of-the-art Li-ion battery is beginning to plateau with respect to its energy density. Promising next-generation battery chemistries, such as magnesium and lithium metal batteries, have the potential to improve capacities by as much as an order of magnitude over Li-ion cells. However, metallic anode materials suffer from detrimental interactions with the battery electrolyte. In this dissertation, we have analyzed several anode/electrolyte challenges for Mg and Li metal batteries at an atomistic model using first-principles computation. Our results clarify some of the fundamental constraints associated with each technology.

6.1 Magnesium metal batteries

A key challenge in Mg metal batteries is electrolyte decomposition on the Mg anode surface. In Chapter 3, we determined likely solvent decomposition products on model Mg anode surface compositions (Mg metal, MgO, and $MgCl_2$) following chemical reaction with a DME solvent molecule. (DME is a prototype solvent used in Mg-based batteries.) We showed that the pristine Mg metal surface is highly prone to reaction with the solvent from thermodynamic and kinetic considerations, leading to the evolution of gas-phase ethylene from the surface. Conversely, on the oxide and chloride surfaces, chemical reaction with the DME molecule is thermoneutral and kinetically hindered, suggesting that these two surfaces are relatively inert. The susceptibility to reaction on the Mg metal surface is a consequence of the ability of the surface to transfer charge to the decomposed DME fragments. MgO and $MgCl_2$ surface films, on the other hand, displayed a tendency to block the transfer of charge with the decomposed fragments.

The following consequences for Mg anode/electrolyte interfaces were drawn:

1. Exposed Mg metal, either due to recently deposited Mg metal or exposed from cracking/exfoliation of an existing SEI, will decompose to ethylene gas upon reaction with DME.
2. Adsorbed fragments on the surface from previous electrolyte decomposition reactions (e.g., oxides and chlorides) are likely to hinder further solvent decomposition.
3. The microstructural and transport properties of these films will determine their utility on the Mg anode surface (i.e., whether or not they allow for Mg-ion migration during plating/stripping).
4. In Cl-containing electrolytes, our work supports the hypothesis that a Mg–Cl enhancement layer may lead to improved electrochemical properties by preventing solvent decomposition. Further, due to the layered (vdW) structure of crystalline $MgCl_2$, potentially allowing for fast ion transport, $MgCl_2$ may be a promising material in a surface film on the Mg anode.

6.2 Lithium metal batteries

In lithium chemistries, an SEI is known to form on the surface of the negative electrode. The composition of the SEI depends strongly on the composition of the electrolyte. Although the SEI has been a topic of research for several years, understanding how the SEI forms and creating batteries with an SEI that prevents electrolyte decomposition and allows for Li^+ transport remains a challenge. In addition, Li (metal) batteries are plagued by dendrite formation due to the uneven plating/stripping of Li ions. In Chapter 4, one potential solution to these problems was posed – employing a 2D, protective graphene oxide membrane on the Li anode. This membrane has been suggested to prevent direct interaction between the anode and the electrolyte, allow for Li-ion transport, and to provide a mechanical barrier to suppress dendrite nucleation. In that chapter, one component of the GO membrane, its adhesive strength, was analyzed as part of a larger study assessing the various properties of a GO membrane (not included in this dissertation). We showed that the GO membrane strongly adheres to the Li surface, a finding supporting its use as a protective layer.

Although it is difficult to predict the composition of an SEI at a Li metal anode, one component that is expected to be universal across all SEIs is the native oxide layer, Li_2O, that forms on Li metal. The native oxide layer is a critical feature controlling the overall properties of an SEI, but its role in LMBs has rarely been explicitly investigated. In Chapter 5, we developed rigorous

models for the native oxide layer using AIMD and DFT. Using an array of structural analysis techniques, including charge transfer and core-level binding energy shifts, we showed how the progression of oxidation on a Li metal film can be quantitatively assessed. Charge transfer and core-level shifts were able to capture the local environment of Li atoms, allowing us to distinguish the transition between Li^0 atoms in the metallic film to Li^+ ions in the oxidized film. Comparing results between an amorphous structure and a crystalline model, the crystalline model displayed a more abrupt transition from metal to oxide at the interface. Further, we computed the Li-ion transport properties from our models of the native oxide layer. The results suggested that a thin native oxide layer is likely to support the fast diffusion of Li ions.

6.3 Future work

With regard to Mg metal batteries, in this dissertation surface films have been shown to have some beneficial properties. Namely, they have the potential to hinder solvent decomposition. On the other hand, surface films also have the potential to prevent the transport of Mg^{2+} across the anode/electrolyte interface, hindering battery performance. Going forward, it would be helpful to determine how, at a fundamental level, Mg^{2+} desolvates from the electrolyte and is transported through plausible Mg anode surface films. An improved understanding of these processes will help answer some of the open questions for Mg batteries, such as: does the presence of a surface layer on a Mg anode fundamentally limit the ability of Mg^{2+} to be transported to the anode, or is there a surface composition(s) that can both block solvent decomposition and allow Mg ions to pass through? There is currently no consensus in the experimental literature on this question: Aurbach and co-workers, for instance, believe that the presence of a surface layer on a Mg anode would block the transport of Mg ions, preventing the battery from being cycled.[7] On the other hand, other work has suggested improved battery performance in the presence of a surface layer.[16]

Regarding Li metal batteries, in this dissertation rigorous models for the native oxide layer on Li metal were developed. The model was explored to compute properties relevant to battery performance (i.e., Li-ion diffusivities). In future work, it would be beneficial to relate structural parameters of the interface with transport properties (i.e., develop structure-property relationships). Further, using the models developed in this work as a foundation, it would be interesting to probe other properties relevant to battery performance such as: what are the dominant diffusion mechanisms in the native oxide layer and how do mechanical properties affect Li-ion

transport? Ultimately, this work would aid researchers in determining if and how the native oxide layer can be modified to improve battery performance.

References

(1) Mohtadi, R.; Mizuno, F. Magnesium Batteries: Current State of the Art, Issues and Future Perspectives. *Beilstein J. Nanotechnol.* **2014**, *5*, 1291–1311.

(2) Zu, C.-X.; Li, H. Thermodynamic Analysis on Energy Densities of Batteries. *Energy Environ. Sci.* **2011**, *4*, 2614.

(3) Kumar, N.; Siegel, D. J. Interface-Induced Renormalization of Electrolyte Energy Levels in Magnesium Batteries. *J. Phys. Chem. Lett.* **2016**, *7* (5), 874–881.

(4) Marom, R.; Amalraj, S. F.; Leifer, N.; Jacob, D.; Aurbach, D. A Review of Advanced and Practical Lithium Battery Materials. *J. Mater. Chem.* **2011**, *21*, 9938–9954.

(5) Goodenough, J. B.; Kim, Y. Challenges for Rechargeable Li Batteries. *Chem. Mater.* **2010**, *22* (3), 587–603.

(6) Liu, Z.; Qi, Y.; Lin, Y. X.; Chen, L.; Lu, P.; Chen, L. Q. Interfacial Study on Solid Electrolyte Interphase at Li Metal Anode : Implication for Li Dendrite Growth. *J. Electrochem. Soc.* **2016**, *163* (3), 592–598.

(7) Yoo, H. D.; Shterenberg, I.; Gofer, Y.; Gershinsky, G.; Pour, N.; Aurbach, D. Mg Rechargeable Batteries: An on-Going Challenge. *Energy Environ. Sci.* **2013**, *6* (8), 2265–2279.

(8) Lu, Z.; Schechter, A.; Moshkovich, M.; Aurbach, D. On the Electrochemical Behavior of Magnesium Electrodes in Polar Aprotic Electrolyte Solutions. *J. Electroanal. Chem.* **1999**, *466* (2), 203–217.

(9) Barile, C. J.; Barile, E. C.; Zavadil, K. R.; Nuzzo, R. G.; Gewirth, A. A. Electrolytic Conditioning of a Magnesium Aluminum Chloride Complex for Reversible Magnesium Deposition. *J. Phys. Chem. C* **2014**, *118* (48), 27623–27630.

(10) Canepa, P.; Gautam, G. S.; Malik, R.; Jayaraman, S.; Rong, Z.; Zavadil, K. R.; Persson, K.; Ceder, G. Understanding the Initial Stages of Reversible Mg Deposition and Stripping in Inorganic Nonaqueous Electrolytes. *Chem. Mater.* **2015**, *27* (9), 3317–3325.

(11) Vardar, G.; Sleightholme, A. E. S.; Naruse, J.; Hiramatsu, H.; Siegel, D. J.; Monroe, C. W. Electrochemistry of Magnesium Electrolytes in Ionic Liquids for Secondary Batteries. *ACS Appl. Mater. Interfaces* **2014**, *6* (20), 18033–18039.

(12) Tutusaus, O.; Mohtadi, R.; Arthur, T. S.; Mizuno, F.; Nelson, E. G.; Sevryugina, Y. V. An Efficient Halogen-Free Electrolyte for Use in Rechargeable Magnesium Batteries. *Angew. Chemie Int. Ed.* **2015**, *54* (27), 7900–7904.

(13) Pour, N.; Gofer, Y.; Major, D. T.; Aurbach, D. Structural Analysis of Electrolyte Solutions for Rechargeable Mg Batteries by Stereoscopic Means and DFT Calculations. *J. Am. Chem. Soc.* **2011**, *133*, 6270–6278.

(14) Connell, J. G.; Genorio, B.; Lopes, P. P.; Strmcnik, D.; Stamenkovic, V. R.; Markovic, N. M. Tuning the Reversibility of Mg Anodes via Controlled Surface Passivation by H2O/Cl- in Organic Electrolytes. *Chem. Mater.* **2016**, *28* (22), 8268–8277.

(15) Tutusaus, O.; Mohtadi, R.; Singh, N.; Arthur, T. S.; Mizuno, F. Study of Electrochemical Phenomena Observed at the Mg Metal/Electrolyte Interface. *ACS Energy Lett.* **2017**, *2* (1), 224–229.

(16) Esbenshade, J. L.; Barile, C. J.; Fister, T. T.; Bassett, K. L.; Fenter, P.; Nuzzo, R. G.; Gewirth, A. a. Improving Electrodeposition of Mg through an Open Circuit Potential Hold. *J. Phys. Chem. C* **2015**, *119* (41), 23366–23372.
(17) Kozen, A. C.; Lin, C.-F.; Zhao, O.; Lee, S. B.; Rubloff, G. W.; Noked, M. Stabilization of Lithium Metal Anodes by Hybrid Artificial Solid Electrolyte Interphase. *Chem. Mater.* **2017**, *29* (15), 6298–6307.
(18) Fan, L.; Zhuang, H. L.; Gao, L.; Lu, Y.; Archer, L. A. Regulating Li Deposition at Artificial Solid Electrolyte Interphases. *J. Mater. Chem. A* **2017**, *5* (7), 3483–3492.
(19) Chen, L.; Connell, J. G.; Nie, A.; Huang, Z.; Zavadil, K. R.; Klavetter, K. C.; Yuan, Y.; Sharifi-Asl, S.; Shahbazian-Yassar, R.; Libera, J. A.; Mane, A. U.; Elam, J. W. Lithium Metal Protected by Atomic Layer Deposition Metal Oxide for High Performance Anodes. *J. Mater. Chem. A* **2017**, *5* (24), 12297–12309.
(20) Kozen, A. C.; Lin, C.-F.; Pearse, A. J.; Schroeder, M. A.; Han, X.; Hu, L.; Lee, S. B.; Rubloff, G. W.; Noked, M. Next-Generation Lithium Metal Anode Engineering via Atomic Layer Deposition. *ACS Nano* **2015**, *9* (6), 5884–5892.
(21) Kazyak, E.; Wood, K. N.; Dasgupta, N. P. Improved Cycle Life and Stability of Lithium Metal Anodes through Ultrathin Atomic Layer Deposition Surface Treatments. *Chem. Mater.* **2015**, *27* (18), 6457–6462.
(22) Zhou, W.; Wang, S.; Li, Y.; Xin, S.; Manthiram, A.; Goodenough, J. B. Plating a Dendrite-Free Lithium Anode with a Polymer/Ceramic/Polymer Sandwich Electrolyte. *J. Am. Chem. Soc.* **2016**, *138* (30), 9385–9388.
(23) Ma, G.; Wen, Z.; Wang, Q.; Shen, C.; Jin, J.; Wu, X. Enhanced Cycle Performance of a Li-S Battery Based on a Protected Lithium Anode. *J. Mater. Chem. A* **2014**, *2*, 19355–19359.
(24) Choi, S. M.; Kang, I. S.; Sun, Y.-K.; Song, J.-H.; Chung, S.-M.; Kim, D.-W. Cycling Characteristics of Lithium Metal Batteries Assembled with a Surface Modified Lithium Electrode. *J. Power Sources* **2013**, *244*, 363–368.
(25) Zheng, G.; Lee, S. W.; Liang, Z.; Lee, H. W.; Yan, K.; Yao, H.; Wang, H.; Li, W.; Chu, S.; Cui, Y. Interconnected Hollow Carbon Nanospheres for Stable Lithium Metal Anodes. *Nat. Nanotechnol.* **2014**, *9*, 618–623.
(26) Pan, J.; Zhang, Q.; Xiao, X.; Cheng, Y.-T.; Qi, Y. Design of Nanostructured Heterogeneous Solid Ionic Coatings through a Multiscale Defect Model. *ACS Appl. Mater. Interfaces* **2016**, *8* (8), 5687–5693.
(27) Wilkening, M.; Indris, S.; Heitjans, P. Heterogeneous Lithium Diffusion in Nanocrystalline Li2O:Al2O3 Composites. *Phys. Chem. Chem. Phys.* **2003**, *5* (11), 2225–2231.
(28) Yan, K.; Lee, H. W.; Gao, T.; Zheng, G.; Yao, H.; Wang, H.; Lu, Z.; Zhou, Y.; Liang, Z.; Liu, Z.; Chu, S.; Cui, Y. Ultrathin Two-Dimensional Atomic Crystals as Stable Interfacial Layer for Improvement of Lithium Metal Anode. *Nano Lett.* **2014**, *14*, 6016–6022.
(29) Huang, J.-Q.; Zhuang, T.-Z.; Zhang, Q.; Peng, H.-J.; Chen, C.-M.; Wei, F. Permselective Graphene Oxide Membrane for Highly Stable and Anti-Self-Discharge Lithium–Sulfur Batteries. *ACS Nano* **2015**, *9*, 3002–3011.
(30) Zhang, Y.; Xia, X.; Wang, D.; Wang, X.; Gu, C.; Tu, J. Integrated Reduced Graphene Oxide Multilayer/Li Composite Anode for Rechargeable Lithium Metal Batteries. *RSC Adv.* **2016**, *6*, 11657–11664.
(31) Lin, D.; Liu, Y.; Liang, Z.; Lee, H. W.; Sun, J.; Wang, H.; Yan, K.; Xie, J.; Cui, Y. Layered Reduced Graphene Oxide with Nanoscale Interlayer Gaps as a Stable Host for Lithium Metal Anodes. *Nat. Nanotechnol.* **2016**, *11*, 626–632.
(32) Zhuang, T.-Z.; Huang, J.-Q.; Peng, H.-J.; He, L.-Y.; Cheng, X.-B.; Chen, C.-M.; Zhang, Q. Rational Integration of Polypropylene/Graphene Oxide/Nafion as Ternary-Layered

Separator to Retard the Shuttle of Polysulfides for Lithium-Sulfur Batteries. *Small* **2016**, *12*, 381–389.
(33) Adams, B. D.; Carino, E. V.; Connell, J. G.; Han, K. S.; Cao, R.; Chen, J.; Zheng, J.; Li, Q.; Mueller, K. T.; Henderson, W. A.; Zhang, J. G. Long Term Stability of Li-S Batteries Using High Concentration Lithium Nitrate Electrolytes. *Nano Energy* **2017**, *40* (September), 607–617.
(34) Li, Y.; Li, Y.; Pei, A.; Yan, K.; Sun, Y.; Wu, C.-L.; Joubert, L.-M.; Chin, R.; Koh, A. L.; Yu, Y.; Perrino, J.; Butz, B.; Chu, S.; Cui, Y. Atomic Structure of Sensitive Battery Materials and Interfaces Revealed by Cryo–Electron Microscopy. *Science.* **2017**, *358* (6362), 506–510.
(35) Gu, Y.; Wang, W.-W.; Li, Y.-J.; Wu, Q.-H.; Tang, S.; Yan, J.-W.; Zheng, M.-S.; Wu, D.-Y.; Fan, C.-H.; Hu, W.-Q.; Chen, Z.-B.; Fang, Y.; Zhang, Q.-H.; Dong, Q.-F.; Mao, B.-W. Designable Ultra-Smooth Ultra-Thin Solid-Electrolyte Interphases of Three Alkali Metal Anodes. *Nat. Commun.* **2018**, *9*, 1339.
(36) Liu, Y.; Lin, D.; Li, Y.; Chen, G.; Pei, A.; Nix, O.; Li, Y.; Cui, Y. Solubility-Mediated Sustained Release Enabling Nitrate Additive in Carbonate Electrolytes for Stable Lithium Metal Anode. *Nat. Commun.* **2018**, *9*, 3656.
(37) Tang, C.-Y.; Dillon, S. J. In Situ Scanning Electron Microscopy Characterization of the Mechanism for Li Dendrite Growth. *J. Electrochem. Soc.* **2016**, *163* (8), A1660–A1665.
(38) Ryou, M. H.; Lee, Y. M.; Lee, Y.; Winter, M.; Bieker, P. Mechanical Surface Modification of Lithium Metal: Towards Improved Li Metal Anode Performance by Directed Li Plating. *Adv. Funct. Mater.* **2015**, *25* (6), 834–841.
(39) Shiraishi, S.; Kanamura, K.; Takehara, Z. Influence of Initial Surface Condition of Lithium Metal Anodes on Surface Modification with HF. *J. Appl. Electrochem.* **1999**, *29* (7), 869–881.
(40) Hong, S.-T.; Kim, J.-S.; Lim, S.-J.; Yoon, W. Y. Surface Characterization of Emulsified Lithium Powder Electrode. *Electrochim. Acta* **2004**, *50*, 535–539.
(41) Kanamura, K.; Shiraishi, S.; Tamura, H.; Takehara, Z. X-Ray Photoelectron Spectroscopic Analysis and Scanning Electron Microscopic Observation of the Lithium Surface Immersed in Nonaqueous Solvents. *J. Electrochem. Soc.* **1994**, *141* (9), 2379.
(42) Cheng, X.-B.; Zhang, R.; Zhao, C.-Z.; Wei, F.; Zhang, J.-G.; Zhang, Q. A Review of Solid Electrolyte Interphases on Lithium Metal Anode. *Adv. Sci.* **2016**, *3* (3), 1500213.
(43) Sholl, D. S.; Steckel, J. A. *Density Functional Theory*; **2009**.
(44) Hohenberg, P.; Kohn, W. Inhomogeneous Electron Gas. *Phys. Rev.* **1964**, *136*, B864–B871.
(45) Kohn, W.; Sham, L. J. Self-Consistent Equations Including Exchange and Correlation Effects. *Phys. Rev.* **1965**, *140*, A1133–A1138.
(46) Perdew, J. P.; Burke, K.; Ernzerhof, M.; of Physics, D.; Quantum Theory Group Tulane University, N. O. L. 70118 J. Generalized Gradient Approximation Made Simple. *Phys. Rev. Lett.* **1996**, *77* (18), 3865–3868.
(47) Kresse, G.; Furthmüller, J. Efficiency of Ab-Initio Total Energy Calculations for Metals and Semiconductors Using a Plane-Wave Basis Set. *Comput. Mater. Sci.* **1996**, *6* (1), 15–50.
(48) Kresse, G.; Furthmüller, J. Efficient Iterative Schemes for Ab Initio Total-Energy Calculations Using a Plane-Wave Basis Set. *Physical Review B*. **1996**, *54*, pp 11169–11186.
(49) Kresse, G.; Hafner, J. Ab Initio Molecular Dynamics for Liquid Metals. *Phys. Rev. B* **1993**, *47* (1), 558–561.
(50) Kresse, G.; Hafner, J. Ab Initio Molecular-Dynamics Simulation of the Liquid-Metal–Amorphous-Semiconductor Transition in Germanium. *Phys. Rev. B* **1994**, *49* (20), 14251–

14269.
(51) Kresse, G.; Joubert, D. From Ultrasoft Pseudopotentials to the Projector Augmented-Wave Method. *Physical Review B*. **1999**, *59*, pp 1758–1775.
(52) Blöchl, P. E. Projector Augmented-Wave Method. *Phys. Rev. B* **1994**, *50* (24), 17953–17979.
(53) Jónsson, H.; Mills, G.; Jacobsen, K. W. Nudged Elastic Band Method for Finding Minimum Energy Paths of Transitions. In *Classical And Quantum Dynamics In Condensed Phase Simulations*; **1998**; pp 385–404.
(54) Köhler, L.; Kresse, G. Density Functional Study of CO on Rh(111). *Phys. Rev. B* **2004**, *70* (16), 165405.
(55) Zeng, Z.; Ma, X.; Ding, W.; Li, W. First-Principles Calculation of Core-Level Binding Energy Shift in Surface Chemical Processes. *Sci. China Chem.* **2010**, *53*, 402–410.
(56) Povey, A. F.; Sherwood, P. M. A. Covalent Character of Lithium Compounds Studied by X-Ray Photoelectron Spectroscopy. *J. Chem. Soc. Faraday Trans. 2* **1974**, *70*, 1240–1246.
(57) J.P., C.; A., S.; M., F.; M., G.; J., T.; D., W. No Title. *J. Microsc. Spectrosc. Electron.* **1979**, *4*, 483.
(58) Suo, L.; Hu, Y.-S.; Li, H.; Armand, M.; Chen, L. A New Class of Solvent-in-Salt Electrolyte for High-Energy Rechargeable Metallic Lithium Batteries. *Nat. Commun.* **2013**, *4*, 1481.
(59) Yao, K. P. C.; Kwabi, D. G.; Quinlan, R. A.; Mansour, A. N.; Grimaud, A.; Lee, Y.-L.; Lu, Y.-C.; Shao-Horn, Y. Thermal Stability of Li 2 O 2 and Li 2 O for Li-Air Batteries: In Situ XRD and XPS Studies. *J. Electrochem. Soc.* **2013**, *160*, A824–A831.
(60) Ota, H.; Sakata, Y.; Wang, X.; Sasahara, J.; Yasukawa, E. Characterization of Lithium Electrode in Lithium Imides/Ethylene Carbonate and Cyclic Ether Electrolytes. *J. Electrochem. Soc.* **2004**, *151*, A437–A446.
(61) Lu, Y.-C.; Crumlin, E. J.; Veith, G. M.; Harding, J. R.; Mutoro, E.; Baggetto, L.; Dudney, N. J.; Liu, Z.; Shao-Horn, Y. In Situ Ambient Pressure X-Ray Photoelectron Spectroscopy Studies of Lithium-Oxygen Redox Reactions. *Sci. Rep.* **2012**, *2*, 715.
(62) Yen, S. P. S.; Shen, D.; Vasquez, R. P.; Grunthaner, F. J.; Somoano, R. B. Chemical and Morphological Characteristics of Lithium Electrode Surfaces. *J. Electrochem. Soc.* **1981**, *128*, 1434–1438.
(63) Mallinson, C. F.; Castle, J. E.; Watts, J. F. Analysis of the Li KLL Auger Transition on Freshly Exposed Lithium and Lithium Surface Oxide by AES. *Surf. Sci. Spectra* **2013**, *20*, 113–127.
(64) Aurbach, D.; Pollak, E.; Elazari, R.; Salitra, G.; Kelley, C. S.; Affinito, J. On the Surface Chemical Aspects of Very High Energy Density, Rechargeable Li–Sulfur Batteries. *J. Electrochem. Soc.* **2009**, *156*, A694–A702.
(65) Wu, Q.-H.; Thissen, A.; Jaegermann, W. Photoelectron Spectroscopic Study of Li Oxides on Li Over-Deposited V 2 O 5 Thin Film Surfaces. *Appl. Surf. Sci.* **2005**, *250*, 57–62.
(66) Marino, C.; Darwiche, A.; Dupré, N.; Wilhelm, H. A.; Lestriez, B.; Martinez, H.; Dedryvère, R.; Zhang, W.; Ghamouss, F.; Lemordant, D.; Monconduit, L. Study of the Electrode/Electrolyte Interface on Cycling of a Conversion Type Electrode Material in Li Batteries. *J. Phys. Chem. C* **2013**, *117*, 19302–19313.
(67) Wagner, C. D.; Muilenberg, G. E. *Handbook of X-Ray Photoelectron Spectroscopy: A Reference Book of Standard Data for Use in X-Ray Photoelectron Spectroscopy*; **1979**.
(68) Surface State Analysis without Exposure to Atmosphere "XPS, AES." https://www.jfe-tec.co.jp/en/battery/case/09.html (accessed Nov 27, 2018).
(69) An, S. J.; Li, J.; Sheng, Y.; Daniel, C.; Wood, D. L. Long-Term Lithium-Ion Battery Performance Improvement via Ultraviolet Light Treatment of the Graphite Anode. *J.*

Electrochem. Soc. **2016**, *163*, A2866–A2875.
(70) Ismail, I.; Noda, A.; Nishimoto, A.; Watanabe, M. XPS Study of Lithium Surface after Contact with Lithium-Salt Doped Polymer Electrolytes. *Electrochim. Acta* **2001**, *46*, 1595–1603.
(71) Cheng, L.; Crumlin, E. J.; Chen, W.; Qiao, R.; Hou, H.; Franz Lux, S.; Zorba, V.; Russo, R.; Kostecki, R.; Liu, Z.; Persson, K.; Yang, W.; Cabana, J.; Richardson, T.; Chen, G.; Doeff, M. The Origin of High Electrolyte–Electrode Interfacial Resistances in Lithium Cells Containing Garnet Type Solid Electrolytes. *Phys. Chem. Chem. Phys.* **2014**, *16*, 18294–18300.
(72) Kanamura, K.; Tamura, H.; Takehara, Z. XPS Analysis of a Lithium Surface Immersed in Propylene Carbonate Solution Containing Various Salts. *J. Electroanal. Chem.* **1992**, *333* (1–2), 127–142.
(73) Dedryvère, R.; Gireaud, L.; Grugeon, S.; Laruelle, S.; Tarascon, J.-M.; Gonbeau, D. Characterization of Lithium Alkyl Carbonates by X-Ray Photoelectron Spectroscopy: Experimental and Theoretical Study. *J. Phys. Chem. B* **2005**, *109*, 15868–15875.
(74) Kanamura, K.; Tamura, H.; Shiraishi, S.; Takehara, Z.-I. XPS Analysis for the Lithium Surface Immersed in γ-Butyrolactone Containing Various Salts. *Electrochim. Acta* **1995**, *40*, 913–921.
(75) Shchukarev, A.; Korolkov, D. XPS Study of Group IA Carbonates. *Open Chem.* **2004**, *2*, 347–362.
(76) A graph of strength versus distance for the 12-6 Lennard-Jones potential https://en.wikipedia.org/wiki/Lennard-Jones_potential#/media/File:12-6-Lennard-Jones-Potential.svg (accessed Nov 27, 2018).
(77) He, X.; Zhu, Y.; Epstein, A.; Mo, Y. Statistical Variances of Diffusional Properties from Ab Initio Molecular Dynamics Simulations. *npj Comput. Mater.* **2018**, *4*, 18.
(78) Wetzel, D. J.; Malone, M. a.; Haasch, R. T.; Meng, Y.; Vieker, H.; Hahn, N. T.; Gölzhäuser, A.; Zuo, J.-M.; Zavadil, K. R.; Gewirth, A. a.; Nuzzo, R. G. Passivation Dynamics in the Anisotropic Deposition and Stripping of Bulk Magnesium Electrodes During Electrochemical Cycling. *ACS Appl. Mater. Interfaces* **2015**, *7*, 18406-18414.
(79) See, K. A.; Chapman, K. W.; Zhu, L.; Wiaderek, K. M.; Borkiewicz, O. J.; Barile, C. J.; Chupas, P. J.; Gewirth, A. A. The Interplay of Al and Mg Speciation in Advanced Mg Battery Electrolyte Solutions. *J. Am. Chem. Soc.* **2016**, *138* (1), 328–337.
(80) Sa, N.; Pan, B.; Saha-Shah, A.; Hubaud, A. A.; Vaughey, J. T.; Baker, L. A.; Liao, C.; Burrell, A. K. Role of Chloride for a Simple, Non-Grignard Mg Electrolyte in Ether-Based Solvents. *ACS Appl. Mater. Interfaces* **2016**, *8* (25), 16002–16008.
(81) Pan, B.; Huang, J.; He, M.; Brombosz, S. M.; Vaughey, J. T.; Zhang, L.; Burrell, A. K.; Zhang, Z.; Liao, C. The Role of $MgCl_2$ as a Lewis Base in ROMgCl-$MgCl_2$ Electrolytes for Magnesium-Ion Batteries. *ChemSusChem* **2016**, *9* (6), 595–599.
(82) Kumar, N.; Radin, M. D.; Wood, B. C.; Ogitsu, T.; Siegel, D. J. Surface-Mediated Solvent Decomposition in Li–Air Batteries: Impact of Peroxide and Superoxide Surface Terminations. *J. Phys. Chem. C* **2015**, *119* (17), 9050–9060.
(83) Kumar, N.; Leung, K.; Siegel, D. J. Crystal Surface and State of Charge Dependencies of Electrolyte Decomposition on LiMn2O4 Cathode. *J. Electrochem. Soc.* **2014**, *161* (8), E3059–E3065.
(84) Samuel, D.; Steinhauser, C.; Smith, J. G.; Kaufman, A.; Radin, M. D.; Naruse, J.; Hiramatsu, H.; Siegel, D. J. Ion Pairing and Diffusion in Magnesium Electrolytes Based on Magnesium Borohydride. *ACS Appl. Mater. Interfaces* **2017**, *9* (50), 43755–43766.
(85) Ha, S.; Lee, Y.-W.; Woo, S. W.; Koo, B.; Kim, J.; Cho, J.; Lee, K. T.; Choi, N.

Magnesium(II) Bis(Trifluoromethane Sulfonyl) Imide-Based Electrolytes with Wide Electrochemical Windows for Rechargeable Magnesium Batteries. *ACS Appl. Mater. Interfaces* **2014**, *6* (6), 4063–4073.
(86) Lee, K.; Murray, É. D.; Kong, L.; Lundqvist, B. I.; Langreth, D. C. Higher-Accuracy van Der Waals Density Functional. *Phys. Rev. B* **2010**, *82* (8), 081101.
(87) Klimeš, J.; Bowler, D. R.; Michaelides, A. Van Der Waals Density Functionals Applied to Solids. *Phys. Rev. B* **2011**, *83* (19), 195131.
(88) Dion, M.; Rydberg, H.; Schröder, E.; Langreth, D. C.; Lundqvist, B. I. Van Der Waals Density Functional for General Geometries. *Phys. Rev. Lett.* **2004**, *92* (24), 246401.
(89) Román-Pérez, G.; Soler, J. M. Efficient Implementation of a van Der Waals Density Functional: Application to Double-Wall Carbon Nanotubes. *Phys. Rev. Lett.* **2009**, *103* (9), 096102.
(90) Credendino, R.; Busico, V.; Causà, M.; Barone, V.; Budzelaar, P. H. M.; Zicovich-Wilson, C. Periodic DFT Modeling of Bulk and Surface Properties of MgCl2. *Phys. Chem. Chem. Phys.* **2009**, *11* (30), 6525–6532.
(91) Tang, J.-J.; Yang, X.-B.; OuYang, L.; Zhu, M.; Zhao, Y.-J. A Systematic First-Principles Study of Surface Energies, Surface Relaxation and Friedel Oscillation of Magnesium Surfaces. *J. Phys. D. Appl. Phys.* **2014**, *47* (11), 115305.
(92) Johansen, C. G.; Huang, H.; Lu, T. M. Diffusion and Formation Energies of Adatoms and Vacancies on Magnesium Surfaces. *Comput. Mater. Sci.* **2009**, *47* (1), 121–127.
(93) Smith, J. G.; Naruse, J.; Hiramatsu, H.; Siegel, D. J. Theoretical Limiting Potentials in Mg/O 2 Batteries. *Chem. Mater.* **2016**, *28* (5), 1390–1401.
(94) Busico, V.; Causà, M.; Cipullo, R.; Credendino, R.; Cutillo, F.; Friederichs, N.; Lamanna, R.; Segre, A.; Van Axel Castelli, V. Periodic DFT and High-Resolution Magic-Angle-Spinning (HR-MAS) 1 H NMR Investigation of the Active Surfaces of MgCl 2 -Supported Ziegler−Natta Catalysts. The MgCl 2 Matrix. *J. Phys. Chem. C* **2008**, *112* (4), 1081–1089.
(95) Acree Jr., W. E.; Chickos, J. S. Phase Transition Enthalpy Measurements of Organic and Organometallic Compounds. In *NIST Chemistry WebBook, NIST Standard Reference Database Number 69, Eds. P.J. Linstrom and W.G. Mallard*; National Institute of Standards and Technology: Gaithersburg, MD, **2016**.
(96) Neugebauer, J.; Scheffler, M. Adsorbate-Substrate and Adsorbate-Adsorbate Interactions of Na and K Adlayers on Al(111). *Phys. Rev. B* **1992**, *46* (24), 16067–16080.
(97) Bader, R. F. W. *Atoms in Molecules - A Quantum Theory*; Oxford University Press: Oxford, **1990**.
(98) Tang, W.; Sanville, E.; Henkelman, G. A Grid-Based Bader Analysis Algorithm without Lattice Bias. *J. Phys. Condens. Matter* **2009**, *21* (8), 084204.
(99) Sanville, E.; Kenny, S. D.; Smith, R.; Henkelman, G. Improved Grid-Based Algorithm for Bader Charge Allocation. *J. Comput. Chem.* **2007**, *28* (5), 899–908.
(100) Henkelman, G.; Arnaldsson, A.; Jónsson, H. A Fast and Robust Algorithm for Bader Decomposition of Charge Density. *Comput. Mater. Sci.* **2006**, *36* (3), 354–360.
(101) Sun, H.; Jin, Z.; Yang, C.; Akkermans, R. L. C.; Robertson, S. H.; Spenley, N. A.; Miller, S.; Todd, S. M. COMPASS II: Extended Coverage for Polymer and Drug-like Molecule Databases. *J. Mol. Model.* **2016**, *22* (2), 47.
(102) Aparicio, S.; Alcalde, R.; Trenzado, J. L.; Caro, M. N.; Atilhan, M. Study of Dimethoxyethane/Ethanol Solutions. *J. Phys. Chem. B* **2011**, *115* (28), 8864–8874.
(103) Laio, A.; Parrinello, M. Escaping Free-Energy Minima. *Proc. Natl. Acad. Sci.* **2002**, *99* (20), 12562–12566.
(104) Laio, A.; Rodriguez-Fortea, A.; Gervasio, F. L.; Ceccarelli, M.; Parrinello, M. Assessing

the Accuracy of Metadynamics. *J. Phys. Chem. B* **2005**, *109* (14), 6714–6721.
(105) Laio, A.; Gervasio, F. L. Metadynamics: A Method to Simulate Rare Events and Reconstruct the Free Energy in Biophysics, Chemistry and Material Science. *Reports Prog. Phys.* **2008**, *71* (12), 126601.
(106) Bucko, T. Ab Initio Calculations of Free-Energy Reaction Barriers. *J. Phys. Condens. Matter* **2008**, *20* (6), 064211.
(107) Roth, P. E.; Orendorff, C. J. How Electrolytes Influence Battery Safety. *Electrochem. Soc. Interface* **2012**, *21* (2), 45–49.
(108) Teng, X.; Zhan, C.; Bai, Y.; Ma, L.; Liu, Q.; Wu, C.; Wu, F.; Yang, Y.; Lu, J.; Amine, K. In Situ Analysis of Gas Generation in Lithium-Ion Batteries with Different Carbonate-Based Electrolytes. *ACS Appl. Mater. Interfaces* **2015**, *7* (41), 22751–22755.
(109) Chen, X.; Hou, T.-Z.; Li, B.; Yan, C.; Zhu, L.; Guan, C.; Cheng, X.-B.; Peng, H.-J.; Huang, J.-Q.; Zhang, Q. Towards Stable Lithium-Sulfur Batteries: Mechanistic Insights into Electrolyte Decomposition on Lithium Metal Anode. *Energy Storage Mater.* **2017**, *8*, 194–201.
(110) Jozwiuk, A.; Berkes, B. B.; Weiß, T.; Sommer, H.; Janek, J.; Brezesinski, T. The Critical Role of Lithium Nitrate in the Gas Evolution of Lithium–Sulfur Batteries. *Energy Environ. Sci.* **2016**, *9* (8), 2603–2608.
(111) Dean, J. A. Section 4; Table 4.5, Electronegativities of the Elements. In *Lange's Handbook of Chemistry (15th Edition)*; McGraw-Hill, **1999**.
(112) Arthur, T. S.; Glans, P.-A.; Singh, N.; Tutusaus, O.; Nie, K.; Liu, Y.-S.; Mizuno, F.; Guo, J.; Alsem, D. H.; Salmon, N. J.; Mohtadi, R. Interfacial Insight from Operando XAS/TEM for Magnesium Metal Deposition with Borohydride Electrolytes. *Chem. Mater.* **2017**, *29* (17), 7183–7188.
(113) Smith, J. G.; Naruse, J.; Hiramatsu, H.; Siegel, D. J. Intrinsic Conductivity in Magnesium-Oxygen Battery Discharge Products: MgO and MgO2. *Chem. Mater.* **2017**, *29* (7), 3152–3163.
(114) Tian, F.; Radin, M. D.; Siegel, D. J. Enhanced Charge Transport in Amorphous Li2O2. *Chem. Mater.* **2014**, *26* (9), 2952–2959.
(115) Perdew, J. P.; Ruzsinszky, A.; Csonka, G. I.; Vydrov, O. A.; Scuseria, G. E.; Constantin, L. A.; Zhou, X.; Burke, K. Restoring the Density-Gradient Expansion for Exchange in Solids and Surfaces. *Phys. Rev. Lett.* **2008**, *100*, 136406.
(116) Cai, W.; Piner, R. D.; Stadermann, F. J.; Park, S.; Shaibat, M. A.; Ishii, Y.; Yang, D.; Velamakanni, A.; An, S. J.; Stoller, M.; An, J.; Chen, D.; Ruoff, R. S. Synthesis and Solid-State NMR Structural Characterization of 13C-Labeled Graphite Oxide. *Science (80-.).* **2008**, *321*, 1815–1817.
(117) Casabianca, L. B.; Shaibat, M. A.; Cai, W. W.; Park, S.; Piner, R.; Ruoff, R. S.; Ishii, Y. NMR-Based Structural Modeling of Graphite Oxide Using Multidimensional 13 C Solid-State NMR and Ab Initio Chemical Shift Calculations. *J. Am. Chem. Soc.* **2010**, *132*, 5672–5676.
(118) Pandey, D.; Reifenberger, R.; Piner, R. Scanning Probe Microscopy Study of Exfoliated Oxidized Graphene Sheets. *Surf. Sci.* **2008**, *602*, 1607–1613.
(119) Adams, J. B.; Hector, Jr, L. G.; Siegel, D. J.; Yu, H.; Zhong, J. Adhesion, Lubrication and Wear on the Atomic Scale. *Surf. Interface Anal.* **2001**, *31*, 619–626.
(120) Siegel, D.; Hector, Jr, L.; Adams, J. Adhesion, Atomic Structure, and Bonding at the Al(111)/α-Al2O3(0001) Interface: A First Principles Study. *Phys. Rev. B* **2002**, *65* (8), 1–19.
(121) Siegel, D. J.; Hector, Jr, L. G.; Adams, J. B. First-Principles Study of Metal –

Carbide/Nitride Adhesion: Al/VC vs. Al/VN. *Acta Mater.* **2002**, *50*, 619–631.
(122) Siegel, D. J.; Hector, Jr, L. G.; Adams, J. B. Adhesion, Stability, and Bonding at Metal/Metal-Carbide Interfaces: Al/WC. *Surf. Sci.* **2002**, *498*, 321–336.
(123) Sharafi, A.; Kazyak, E.; Davis, A. L.; Yu, S.; Thompson, T.; Siegel, D. J.; Dasgupta, N. P.; Sakamoto, J. Surface Chemistry Mechanism of Ultra-Low Interfacial Resistance in the Solid-State Electrolyte Li7La3Zr2O12. *Chem. Mater.* **2017**, *29* (18), 7961–7968.
(124) Camacho-Forero, L. E.; Smith, T. W.; Bertolini, S.; Balbuena, P. B. Reactivity at the Lithium–Metal Anode Surface of Lithium–Sulfur Batteries. *J. Phys. Chem. C* **2015**, *119*, 26828–26839.
(125) Camacho-Forero, L. E.; Balbuena, P. B. Elucidating Electrolyte Decomposition under Electron-Rich Environments at the Lithium-Metal Anode. *Phys. Chem. Chem. Phys.* **2017**, *19* (45), 30861–30873.
(126) Soto, F. A.; Ma, Y.; Martinez De La Hoz, J. M.; Seminario, J. M.; Balbuena, P. B. Formation and Growth Mechanisms of Solid-Electrolyte Interphase Layers in Rechargeable Batteries. *Chem. Mater.* **2015**, *27* (23), 7990–8000.
(127) Wan, G.; Guo, F.; Li, H.; Cao, Y.; Ai, X.; Qian, J.; Li, Y.; Yang, H. Suppression of Dendritic Lithium Growth by in Situ Formation of a Chemically Stable and Mechanically Strong Solid Electrolyte Interphase. *ACS Appl. Mater. Interfaces* **2018**, *10* (1), 593–601.
(128) Sharafi, A.; Kazyak, E.; Davis, A. L.; Yu, S.; Thompson, T.; Siegel, D. J.; Dasgupta, N. P.; Sakamoto, J. Surface Chemistry Mechanism of Ultra-Low Interfacial Resistance in the Solid-State Electrolyte Li 7 La 3 Zr 2 O 12. *Chem. Mater.* **2017**, *29* (18), 7961–7968.
(129) Lepley, N. D.; Holzwarth, N. A. W. Modeling Interfaces between Solids: Application to Li Battery Materials. *Phys. Rev. B* **2015**, *92* (21), 214201.
(130) Koch, S. L.; Morgan, B. J.; Passerini, S.; Teobaldi, G. Density Functional Theory Screening of Gas-Treatment Strategies for Stabilization of High Energy-Density Lithium Metal Anodes. *J. Power Sources* **2015**, *296*, 150–161.
(131) Radin, M. D.; Rodriguez, J. F.; Tian, F.; Siegel, D. J. Lithium Peroxide Surfaces Are Metallic, While Lithium Oxide Surfaces Are Not. *J. Am. Chem. Soc.* **2012**, *134* (2), 1093–1103.
(132) Wang, Y.; Liu, Z. K.; Chen, L. Q.; Wolverton, C. First-Principles Calculations of B″-Mg5Si6/α-Al Interfaces. *Acta Mater.* **2007**, *55* (17), 5934–5947.
(133) Zimmermann, J.; Finnis, M. W.; Ciacchi, L. C. Vacancy Segregation in the Initial Oxidation Stages of the TiN(100) Surface. *J. Chem. Phys.* **2009**, *130* (13), 134714.
(134) Nosé, S. A Unified Formulation of the Constant Temperature Molecular Dynamics Methods. *J. Chem. Phys.* **1984**, *81*, 511–519.